

2-8-2011

# Mode I and Mode II Measurements For Stiction Failed Micro-Electro-Mechanical Systems

Maheshwar Kashamolla

Follow this and additional works at: [https://digitalrepository.unm.edu/me\\_etds](https://digitalrepository.unm.edu/me_etds)

---

## Recommended Citation

Kashamolla, Maheshwar. "Mode I and Mode II Measurements For Stiction Failed Micro-Electro-Mechanical Systems." (2011).  
[https://digitalrepository.unm.edu/me\\_etds/48](https://digitalrepository.unm.edu/me_etds/48)

This Thesis is brought to you for free and open access by the Engineering ETDs at UNM Digital Repository. It has been accepted for inclusion in Mechanical Engineering ETDs by an authorized administrator of UNM Digital Repository. For more information, please contact [disc@unm.edu](mailto:disc@unm.edu).

**Maheshwar Reddy Kashamolla**

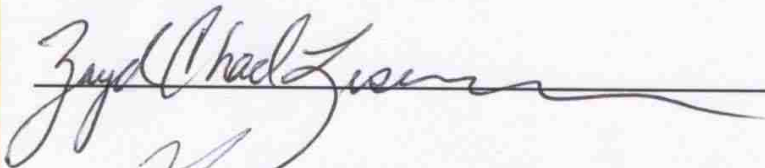
Candidate

**Mechanical Engineering Department**

Department

This thesis is approved, and it is acceptable in quality and form for publication on microfilm:

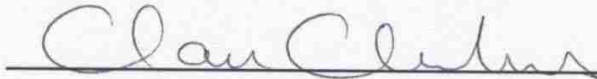
*Approved by the Thesis Committee:*



Dr. Zayd C. Leseman  
(Chairperson)



Dr. Yu-Lin Shen  
(Committee Member)



Dr. Claudia C. Luhrs  
(Committee Member)

\_\_\_\_\_  
\_\_\_\_\_  
\_\_\_\_\_  
\_\_\_\_\_

Accepted:

\_\_\_\_\_  
*Dean, Graduate School*

\_\_\_\_\_  
*Date*

**MODE I AND MODE II MEASUREMENTS FOR STICTION FAILED  
MICRO-ELECTRO-MECHANICAL SYSTEMS**

**BY**

**MAHESHWAR REDDY KASHAMOLLA**

B.Tech., Mechanical Engineering, Jawaharlal Nehru Technological  
University, India, May 2006

THESIS

Submitted in Partial Fulfillment of the  
Requirements for the Degree of

**Master of Science  
Mechanical Engineering**

The University of New Mexico  
Albuquerque, New Mexico

**December, 2010**

## ACKNOWLEDGEMENTS

First and foremost, I would like to express my deepest gratitude to Dr. Zayd C. Leseman, my graduate advisor, who was instrumental in my graduate career. He introduced me to this exciting field of MEMS, provided technical guidance, necessary financial support and overlooked my mistakes. I want to thank him for his continuous support, feedback and constant encouragement through the years of study and research.

I would like to take this opportunity to thank Dr. Yu-Lin Shen and Dr. Claudia C. Luhrs for serving on my advisory committee and for providing their professional expertise.

Most importantly, my parents Amruth Reddy Kashamolla and Pushpa Kashamolla deserve much credit for my success who sacrificed their personal fears of being alone and to be away from their son to see me graduate.

I extend my gratitude to my mother's elder sister Venkatamma for her constant encouragement, unconditional support and genuine love which is the greatest gift of all. I cannot imagine my life without her being an important part of it.

I am also very thankful to my sister and elder brother for their support and love to reach this point in my life. I owe special thanks to my friends Kiranmaye Aluru, Raghavender Uppu, Rajender Reddy Gurralla, and Ramarao Uppuganti, for their continuous support and encouragement in each and every step of my life.

I am thankful to my fellow graduate students, Drew Goettler for his help with using the FIB. In addition, I am also thankful to Arash Mousavi and Khawar Abbas for their help, support and friendship. Our conversations and work together have greatly influenced this thesis. I would like to convey a special thanks to Lance Edens for helping

me with obtaining AFM images and roughness measurements. Most importantly, I want to thank the management and support staff of MTTC, specially Harold Madsen and Sam Kriser.

Last but not the least, I would like to thank God for being there for me in every step that I took to be here far away from my home. I want to thank God for everything that I am blessed with in my Life and for giving me this opportunity to learn and answering my prayers at all times.

**MODE I AND MODE II MEASUREMENTS FOR STICTION FAILED  
MICRO-ELECTRO-MECHANICAL SYSTEMS**

**BY**

**MAHESHWAR REDDY KASHAMOLLA**

**ABSTRACT OF THESIS**

Submitted in Partial Fulfillment of the  
Requirements for the Degree of

**Master of Science  
Mechanical Engineering**

The University of New Mexico  
Albuquerque, New Mexico

**December, 2010**

# **MODE I AND MODE II MEASUREMENTS FOR STICTION FAILED MICRO-ELECTRO-MECHANICAL SYSTEMS**

**BY**

**MAHESHWAR REDDY KASHAMOLLA**

B.Tech., Mechanical Engineering, Jawaharlal Nehru Technological University, 2006  
M.S. Mechanical Engineering, University of New Mexico, 2010

## **ABSTRACT**

Among MicroElectroMechanical Systems (MEMS), the most common type of failure is stiction. Stiction is the unintended adhesion between two surfaces when they are in close proximity to each other. Various studies have been conducted in recent years to study stiction. Our research group has shown the in-service repair of the stiction failed MEMS devices is possible with structural vibrations. In order to further understand this phenomenon and better predict, theoretically, the onset of repair we have constructed an apparatus to determine the Mode I, II, and III interfacial adhesion energies of MEMS devices failed on a substrate. Though our method is general, we are specifically focused on devices created using the SUMMiT V process. An apparatus has been constructed that has 8 degrees-of-freedom between the MEMS device, the surface on which the device is failed, and a scanning interferometric microscope. Deflection profiles of stiction failed MEMS (micro-cantilevered beams 1000 microns long, 30 microns wide, and 2.3 microns thick) have their deflection profiles measured with nanometer resolution by a scanning interferometric microscope. Using the experimental apparatus that is constructed, we determine the Mode I and Mode II interfacial adhesion energies using two methodologies. The first method utilizes the peel test scheme to determine pure Mode-I and Mixed Mode (Mode I and II) interfacial adhesion energies. In order to determine the

values for the interfacial adhesion energies a nonlinear model was developed for the deflection of a beam that accounts for its stretching. Energy methods are then utilized to determine interfacial adhesion energies. Using the same experimental apparatus Mode II interfacial adhesion energies are measured directly with a novel technique developed in this work. This experimental method for measuring the Mode II interfacial adhesion energies for stiction failed MEMS devices uses a microcantilever beam (1500  $\mu\text{m}$  long, 30  $\mu\text{m}$  wide and 2.3  $\mu\text{m}$  thick) attached to MEMS actuator with fix-fix beam flexure. Deflection of the spring is measured with the vernier scale of the actuator. Then a nonlinear elastic model for the fix–fix beam flexure is used to determine the interfacial adhesion energy between the failed microcantilever beam and the surface. A theory is developed to measure the strain energy release rates with finite crack growth, which gives the upper bounds of interfacial adhesion energy for Mode II fracture problem. A separate theory is developed for infinitesimal crack growth, which gives the exact interfacial adhesion energy of the Mode II fracture problem. Because the surface roughness plays an important role in the adhesion of MEMS structures, the surfaces of all structures have been characterized with an Atomic Force Microscope (AFM).



## Table of Contents

LIST OF FIGURES .....	X
LIST OF TABLES.....	XV
CHAPTER 1 .....	1
1 INTRODUCTION.....	1
1.1 Introduction to MEMS.....	1
1.2 Scope.....	5
CHAPTER 2 .....	7
2 THEORY OF MODE I AND MODE II EXPERIMENTS.....	7
2.1 Mode I: Nonlinear Beam Theory.....	7
2.2 Strain Energy Release Rate Formulation.....	12
2.3 Mode II Theory.....	15
2.3.1 Theory to Determine Upper Bounds of $G_{II}$ .....	15
2.3.2 Theory to Determine the Exact Value of $G_{II}$ .....	21
CHAPTER 3 .....	24
3 EXPERIMENTAL SETUP.....	24
3.1 Experimental Setup for Mode I and Mode II.....	24
CHAPTER 4 .....	29
4 EXPERIMENTAL PROCEDURE .....	29
4.1 Experimental Concept and Procedure for Mode I.....	29
4.2 Experimental Procedure for Mode II.....	32
4.2.1 Microcantilever Beams Fabrication.....	33
4.2.2 MEMS Actuator Fabrication.....	34

4.2.3	Experimental Device preparation.....	35
4.3	Experimental Concept for Mode II.....	39
4.3.1	Experimental Concept to Determine Upper Bounds of $G_{II}$ .....	39
4.3.2	Experimental Concept to Determine Exact Value of $G_{II}$ .....	42
CHAPTER 5	.....	45
5	EXPERIMENTAL RESULTS AND DISCUSSION.....	45
5.1	Experimental Results for Mode I.....	45
5.1.1	Modeling Discussion.....	47
5.1.2	Experimental Discussion.....	50
5.1.3	Practical Considerations.....	55
5.2	Experimental Results for Mode II.....	57
5.2.1	Experimental Results for Upper Bounds of $G_{II}$ .....	57
5.2.2	Experimental Results for an Exact Value of $G_{II}$ .....	63
CHAPTER 6	.....	68
6	ROUGHNESS ANALYSIS.....	68
6.1	Roughness Analysis of Microcantilever Beam.....	69
6.2	Roughness Analysis of Substrate.....	73
CHAPTER 7	.....	77
7	CONCLUSIONS.....	77
7.1	Conclusions Drawn from Mode I Experiments.....	77
7.2	Conclusions Drawn from Mode II Experiments and Roughness Analysis ...	78
REFERENCES	.....	79

## LIST OF FIGURES

Figure 1: $\mu$ cantilever beam failed in an <i>s</i> -shaped manner .....	7
Figure 2: At each increment of <i>h</i> , the polysilicon beams studied here can be modeled as fix-fix beams. The free body diagram of the beam includes a bending moment at each end as well as a horizontal and a vertical force. The beam is statically indeterminate.....	8
Figure 3: Comparison between the linear and nonlinear model developed in this work for a fix-fix beam with ends offset by a distance <i>h</i> .....	12
Figure 4: Design of fix-fix flexure.....	16
Figure 5: Free body diagram of the fix-fix beam.....	16
Figure 6: Force versus deflection theoretical curve for a fix-fix beam.....	18
Figure 7: Design of fix-fix beam flexure with cantilever beam attached .....	19
Figure 8: Tensile beam with dimensions .....	20
Figure 9: Tensile beam with a length <i>L</i> , width <i>w</i> and thickness <i>t</i> .....	21
Figure 10: Experimental setup showing the apparatus for measuring Mode I and Mixed Mode adhesion energies.....	25
Figure 11: The physical layout of SUMMiT V <sup>TM</sup> Material Layers with 5 levels of poly-Si and 4 layers of sacrificial oxides.....	27
Figure 12: Schematic representation of experiments for Mode I .....	29
Figure 13: Top-view of the microcantilever beams placed above the substrate.....	31
Figure 14: 3D profile of 1000 $\mu$ m length cantilever beams stiction failed in an <i>s</i> -shaped profile.....	32

Figure 15: Top view of microcantilever beams fabricated with the SUMMiT V <sup>TM</sup> process .....	33
Figure 16: SEM image of the MEMS Actuator device fabricated for Mode II experiments .....	35
Figure 17: SEM image of the $\mu$ cantilever beams used for experimental device preparation .....	36
Figure 18: SEM image of the omniprobe welded to the $\mu$ cantilever beam and is cut loose to transfer onto the MEMS Actuator .....	37
Figure 19: SEM image of the omniprobe transferring the $\mu$ cantilever beam onto the freely moving shuttle of the MEMS Actuator.....	37
Figure 20: SEM image of the $\mu$ cantilever beam welded on the freely moving shuttle of an MEMS Actuator (Pt straps used to weld $\mu$ cantilever and shuttle are seen).....	38
Figure 21: SEM image of a Mode II experimental device with a $\mu$ cantilever beam welded to the MEMS Actuator.....	38
Figure 22: SEM image of an actuator dimensions a) length of the beam b) width of the beam c) height of the beam.....	39
Figure 23: Schematic representation of experiments for Mode II .....	40
Figure 24: Cantilever beam attached to MEMS actuator with fix-fix beams flexure overlapped with the substrate.....	41
Figure 25: SEM image of the vernier scale of the MEMS actuator.....	42
Figure 26: Schematic representation of Mode II experiments to see the infinitesimal crack growth .....	43

Figure 27: Interferometric image showing the cantilever beam raised to  $< \frac{1}{4}$  of beam thickness at the base..... 44

Figure 28: Example of the type of fit attained using the nonlinear model ..... 45

Figure 29: The strain energy release rate increases as the crack propagates with increase in height ..... 46

Figure 30: Longitudinal stress that develops in the  $\mu$ cantilevers as a function of height. 48

Figure 31: The simplest model to study the role of friction is to consider the surfaces to be interlocked as shown. In general not all portions of the contacting surfaces can be modeled to be composed of normal and vertical surfaces but the proposed analysis can be used to attain sufficient insight on the role of friction ..... 52

Figure 32: The friction force on the side faces of the bumps as the slide on top of each other during the crack propagation. The friction force represented here is obtained considering the macroscopic friction coefficient to hold at the microscale ..... 54

Figure 33: The values of  $G_f$  presented here shows the portion of the strain energy release rate that is due to the friction on sliding faces of the bumps. This portion is not due to the elastic strain energy stored in the beam and should be subtracted from the total strain energy calculated.  $G_f$  is not present in macro-scale mode I crack propagation. The reason that it is seen in the macrocantilever test is due to large longitudinal force developed in the cantilever..... 54

Figure 34: Although it was shown that friction is responsible for a considerable portion of  $G$  but even after subtracting  $G_f$  from the total strain energy release rate one

should not expect to get a constant value for strain energy release rate. The reason is due to the effects of loading..... 55

Figure 35: Piezo displacement versus spring displacement curve..... 57

Figure 36: Piezo displacement versus force applied curve..... 58

Figure 37: Piezo displacement versus  $G$  curve ..... 60

Figure 38: An example of two rough surfaces in contact, (a) Larger contact area brought on by capillary forces (b) An image where broken particles acting as ball bearings between the two rough surfaces (c) An image where the broken particles sit in the valley of top rough surface ..... 61

Figure 39: Length of the  $\mu$ cantilever beam versus height raised at fixed end of the beam ..... 63

Figure 40: ROI of figure 39 which shows the crack growth with every increment of piezo ..... 64

Figure 41: Schematic showing the various regions that are characterized ..... 68

Figure 42: AFM image of an experimentally disturbed Poly1 rubbed surface of  $\mu$ cantilever beam..... 70

Figure 43: AFM zoomed-in image of an experimentally disturbed Poly1 rubbed surface of  $\mu$ cantilever beam ..... 70

Figure 44: AFM Roughness Analysis of an experimentally disturbed Poly1 rubbed surface of  $\mu$ cantilever beam..... 71

Figure 45: AFM image of a virgin Poly1 lower surface of  $\mu$ cantilever beam..... 71

Figure 46: AFM Image Zoomed-in image of a virgin Poly1 lower surface of  $\mu$ cantilever beam..... 72

Figure 47: AFM Roughness Analysis of a virgin Poly1 lower surface of  $\mu$ cantilever beam ..... 72

Figure 48: AFM image of the substrate with marked region to identify contact and no contact areas with the bottom side of a  $\mu$ cantilever beam ..... 74

Figure 49: AFM Roughness Analysis of an experimentally disturbed Poly0 surface of the substrate ..... 75

Figure 50: AFM Roughness Analysis of a virgin Poly0 surface of the substrate ..... 75

## LIST OF TABLES

Table 1: Critical strain energy release rate $G_C$ for a wide range of various materials [65]	
.....	66
Table 2: Comparison of Strain Energy Release Rates $G$ .....	67



# CHAPTER 1

## INTRODUCTION

### 1.1 Introduction to MEMS

MEMS continue to be a technology that attracts a huge amount of interest among the engineering community. MEMS is an acronym used to represent Micro-Electro-Mechanical-Systems. MEMS are micro scale machines with moving parts which are invisible to the eye. Mechanical elements, sensors, actuators, and electronics are integrated on a common silicon substrate through microfabrication technology to form MEMS. Typically, silicon wafers are used to build these machines. The great advantage of MEMS technology is the parallel processing that can occur for mass production of devices.

Ever since the first micro machined motors were demonstrated in the mid 1980's, there has been an extensive array of impressive research in MEMS. The transition of this research in to commercial products has been limited due to many manufacturing issues. Some of the commercial products in which these MEMS are used is airbag accelerometers [1] in the automobile industry, optical devices like micro-mirrors [2], hard disk drives [3] for improving the data storage capacity, inkjet printer heads [4], gyroscopes [5], optical switches [6], and security devices [7]. One of the key issues associated with manufacturing of MEMS is stiction. Stiction is the phenomenon wherein two surfaces adhere together when they are in close proximity to each other. Because of the relatively small dimensional scale these devices exist in they tend to have high surface area to volume ratios [8] by thus making them susceptible to stiction. During the fabrication of MEMS devices, the presence of capillary forces may cause the

microstructures to adhere with their substrate [9] or adjacent MEMS structures. The various factors that account to stiction are capillary forces [9], van der Waals forces [10], electrostatic, and/or chemical forces [11], and humidity [12].

Stiction failure can be classified into two types, release stiction and in-use stiction. Fabrication processes are responsible for causing the release stiction. In-use stiction can occur at anytime while the MEMS is in service. Both types of stiction severely affect the reliability of MEMS devices and thus limit the wide spread commercial success of MEMS. A significant amount of research has been performed in order to overcome stiction failure. Investigators have tried to reduce or eliminate stiction. In order to prevent release stiction during the fabrication of MEMS devices, there are many processing techniques [13-21] that are employed. Another method that is used for stiction prevention coating the MEMS devices with self assembled monolayers SAM's [22-30]. This reduces the surface energy of the MEMS devices. All the above methods are very useful to reduce the possibility of stiction, however it is not possible to completely mitigate the onset of in-use stiction using the above methods.

Though some of the above coating procedures have shown some promise for the improvement of production yield and also the performance of the MEMS, there is a need for quantitative measurements of the surface energy to fully understand the effects of the coating strategies on the performance and reliability of the MEMS throughout their service-life.

With the occurrence of in-use stiction, the MEMS device has to be repaired or replaced in order to restore its functionality. As replacement is not always an easy option, it is preferable to repair the MEMS devices. It has been shown that by employing pulsed

lasers [31-34], which causes differential heating of the stiction failed device and its substrate, it is possible to repair stiction failed devices. One limitation with this method was heating of the entire device rather than just the stiction failed portion of the device which can lead to destruction or reduced functionality of the device. Release of stiction failed MEMS with ultrasonic waves has also been attempted [35, 36]. Additionally, inducing stress waves via a pulsed laser [37, 38] has also been shown to repair stiction failed MEMS. However, a more convenient way to repair stiction failed MEMS devices has been demonstrated using structural vibrations [39, 40].

In both the above cases of avoiding or repair of stiction failure, proper design of the method depends on knowledge of the interfacial adhesion energy,  $G$ . Alternate names for this which will be used interchangeably throughout this thesis, are critical strain energy release rate and adhesion energy. Most of the investigators used MEMS structures to study the stiction phenomenon. Mastrangelo and Hsu [41-43] proposed simple methods for calculating the adhesion energy associated with the shortest beam that is stiction-failed using the Cantilever Beam Array (CBA) experiment. By expanding on this approach, a fracture mechanics model was developed by de Boer and Michalske [44] to calculate the adhesion energy. They used crack length as the main parameter to calculate the adhesion energy. Jones *et al.* [45] examined the adhesion of microcantilevers subjected to mechanical point loading by developing the models and the experiments. Leseman *et al.* [46], [47] developed a new technique for accurately measuring the adhesion energy of stiction failed microcantilevers using a cantilever beam peel test. Hurst *et al.* [48] developed a new method to determine adhesion energy of cantilever beams using experimental data of the beams heights. Prior studies [38], [40], [44], [46],

[47] have been performed to calculate Mode I strain energy release rates  $G$  used Cantilever Beam Array (CBA) methods. Herein this method will be referred to as the ‘linear’ method due to the linear nature of the force versus deflection curve found for the deformation of the beam. Using the linear description for the deflection of a beam,  $G$  was found to be

$$G = \frac{3}{2} \frac{h^2 E t^3}{s^4} \quad (1)$$

where  $h$  is the height of the base of the cantilever above the substrate,  $E$  is the elastic modulus,  $t$  is the thickness of the beam, and  $s$  is the length of the beam, not stiction failed onto the substrate. (1) is derived by making the assumptions that the slopes (and rotations) were small and that the deformations are due purely to bending. For stiction failed CBA experiments, in order for the rotations to be small and not to induce elongation in the structure (the cantilevers actually transform into fix-fix beams after failure), the deflection should be less than  $\frac{1}{4}$  of the thickness of the structure [9], [49]. Additionally, when deflections are large, the strain energy due to bending alone may not be sufficient to capture all of strain energy that is imparted onto the beam.

Experimentally, it should be noted that the value for  $G$  is very sensitive to  $s$  and  $h$ . Inspecting (1)  $G \propto h^2/s^4$ . Thus it is imperative to measure  $s$  and  $h$  as accurately as possible.

In an effort to increase the accuracy of the measurement of  $G$ , using the CBA method, a new analysis method has been developed and applied to experiments. Specifically, this work considers the large deflections of the beams through the

development of a nonlinear beam deflection model that does not ignore stretching of the beams. Using the output of the nonlinear deflection model an energy method is derived that includes the effect of all forces in the system as well as the moments, leading to a more accurate value for  $G$ . In order to verify this new methodology, a set of experiments were undertaken that determine  $s$  and  $h$  accurately by utilizing a vertical scanning interferometer.

As experimental studies correlating Mode II failure are not available, a novel technique is developed in this work by which Mode II interfacial adhesion energies are measured directly. Mode II interfacial adhesion energies are represented with  $G_{II}$  throughout this thesis. With the rapidly growing market for micro scale devices, there is a need for the quantitative measurements of  $G$  for both Mode I and Mode II accurately. In order to fully understand the effects of the coating strategies to reduce the stiction or to repair for the performance and reliability of the MEMS throughout their service life. Thus, by realizing the importance of the quantitative measurements  $G$  for stiction failed MEMS devices, Mode I and Mode II experiments were undertaken.

## **1.2 Scope**

The scope of this thesis is to measure and analytically model the strain energy release rates of Mode I and Mode II failure for stiction failed microcantilever beams. Microcantilevers fabricated using SUMMiT V<sup>TM</sup> technology were chosen due to the amount of work previously done in characterizing the critical strain energy release rate of these structures. Additionally, the SUMMiT V<sup>TM</sup> continues to be one of the only publically available MEMS foundaries in the world. Because this process will vary only

slightly as time moves on and anyone can utilize this process experiments and analysis were performed for MEMS created by this process.

## CHAPTER 2

### THEORY OF MODE I AND MODE II EXPERIMENTS

#### 2.1 Mode I: Nonlinear Beam Theory

$\mu$ cantilever beams will fail in one of two failure modes, arc or *s*-shaped [44]. Here our focus is on *s*-shaped stiction failed microcantilever beams which behave as a fixed-guided beam.  $\mu$ cantilever beam failed in an *s*-shaped manner is shown in Figure 1. In order to derive an equation to calculate the strain energy release rate for Mode I and Mode II, it is important to understand the concepts of Mode I and Mode II. For Mode I failure, a force acts normal to the plane of the crack. For Mode II failure, a shear stress acts parallel to the plane of the crack and perpendicular to the crack front.

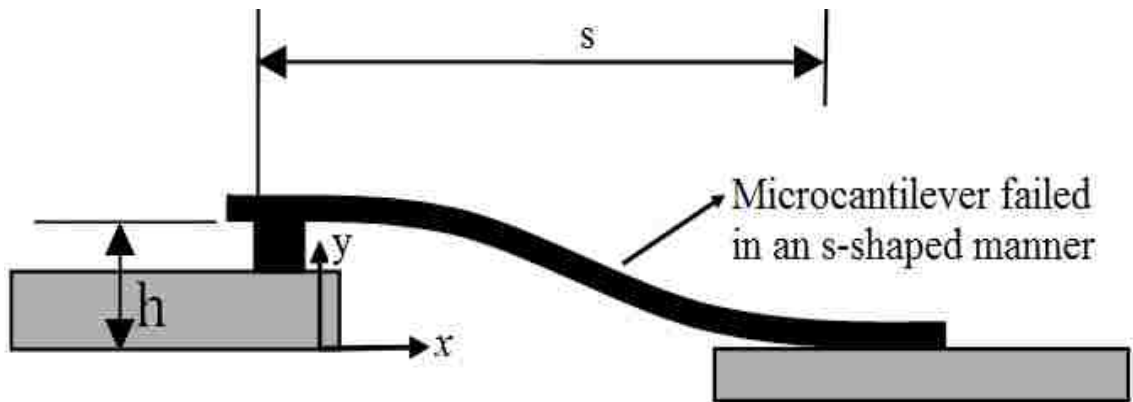


**Figure 1:**  *$\mu$ cantilever beam failed in an s-shaped manner*

In order to determine the critical strain energy release rate the total energy of the adhered beams needs to be found. In absence of external forces acting on the  $\mu$ cantilevers, the total energy of the stiction failed  $\mu$ cantilevers consists of the energy stored due to the deformation of the  $\mu$ cantilevers (not just bending). We typically assume small deformations, small rotations, free slip of the  $\mu$ cantilevers on the substrate, no residual stresses, and smooth surfaces. This leads to the conclusion that deformation of

the beams is only due to bending. However, for cases where the height ( $h$ ) between the end of the beam exceeds  $\frac{1}{4}$  of its thickness, a non-negligible amount of elastic energy is due to stretching of the beam [9], [49]. In absence of the free slip condition, herein a nonlinear model is developed for the deformation of a fixed-guided beam that includes bending and stretching.

The shape of a homogeneous isotropic cantilever beam that has small deflection and rotations is governed by the differential equation of the deflection curve for a beam:

$$M(x) = EIy''(x) \quad (2)$$

where  $M(x)$ , is the bending moment,  $E$ , is Young's modulus of elasticity,  $I$ , is the second moment of inertia and,  $y$ , is the deflection at location  $x$ .

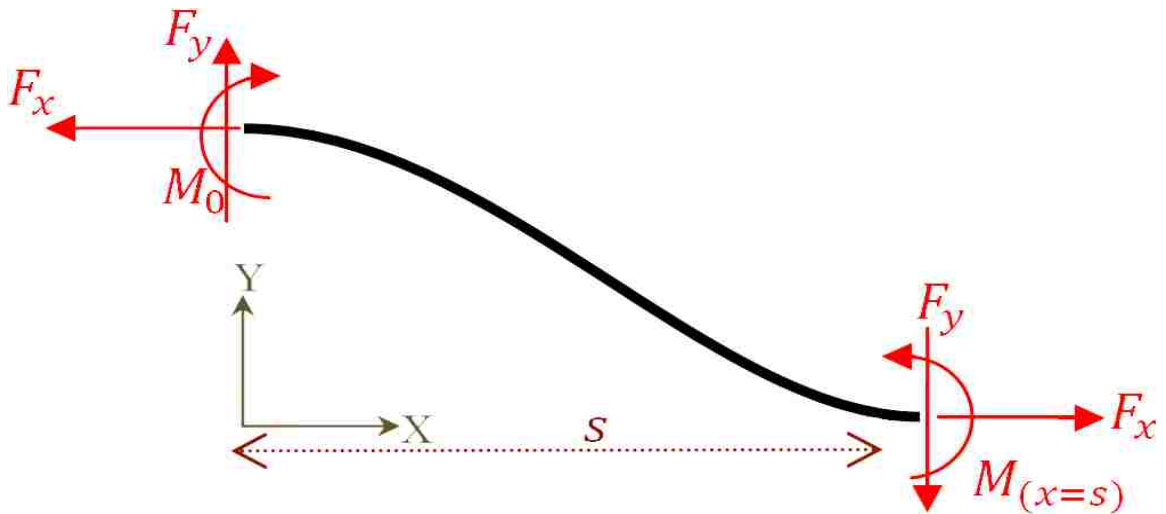


**Figure 2:** At each increment of  $h$ , the polysilicon beams studied here can be modeled as fix-fix beams. The free body diagram of the beam includes a bending moment at each end as well as a horizontal and a vertical force. The beam is statically indeterminate.



Using the free body diagram of the beam (Figure 2) the bending moment at a point  $(x, y)$  is found to be:

$$M = M_0 + F_x y + F_y x \quad (3)$$

where  $M_0$  is the bending moment and  $F_x$  and  $F_y$  are the normal and shear components of the forces at the anchor point. Substituting  $M(x)$  into the curvature equation yields a second order non-homogeneous linear differential equation that has a general solution in the form of:

$$y(x) = c_1 e^{Kx} + c_2 e^{-Kx} - \frac{M_0 + F_y x}{EIK^2} \quad (4)$$

where  $K$  is a dummy parameter defined as  $K = \sqrt{\frac{F_x}{EI}}$ ,  $c_1$  and  $c_2$  are constants that must be determined using the boundary conditions. Boundary conditions for Figure 2 are:

$$y(0) = h$$

$$y(s) = 0$$

$$\theta(0) = 0$$

$$\theta(0) = 0$$

As shown in (5) and (6), using the aforementioned boundary conditions,  $c_1$  and  $c_2$  can be determined as a function of  $K$ .

$$c_1 = \frac{-h}{2 + sK + e^{sK}(sK - 2)} \quad (5)$$

$$c_2 = \frac{e^{sK}h}{2 + sK + e^{sK}(sK - 2)} \quad (6)$$

In these experiments no horizontal displacement is allowed at the anchor points. This constraint makes the beam a first order hyperstatic system by introducing an unknown force  $F_x$  on the beam. In order to solve this system of equations additional knowledge of the mechanical properties and geometry of the beam are employed. Poly-Si is a linear elastic material. As such, Hooke's Law, (7), is invoked in order to determine  $F_x$ . For this work Hooke's Law takes the form:

$$\frac{L - L_0}{L_0} = \frac{F_x}{AE} \quad (7)$$

where  $L$  is the deformed length of the beam,  $L_0$  is the initial length (taken here as  $s$ ), and  $A$  is the cross sectional area of the beam. All variables in (7) are known except  $L$  and  $F_x$ . The deformed shape of the beam is known to be a function of  $F_x$  which affects the length of the beam along its longitudinal axis. The total length of the beam can be calculated by determining the length of the curve defined by (4). Specifically, (8) is used.

$$L = \int_0^s \left( \sqrt{1 + \left( \frac{\partial y(x)}{\partial x} \right)^2} \right) dx \quad (8)$$

(4) - (8) are solved numerically in order to obtain results. The general solution process begins by inputting values for  $s$ ,  $h$ , and  $F_x$ .  $s$  and  $h$  are immediately available from the experimental data, while  $F_x$  must have an initial guess. Note that  $s$  and  $h$  can be left as free parameters with bounds from the experimental error in order to attain more accurate solutions. With these values (4) - (6) can be solved to determine  $y(x)$ . The deformed length is then found using (8). Finally, the left hand side of (7) is solved. This result is compared to the value of the right hand side of (7) with  $F_x$  from solving (4) - (6). If the two are not equal then  $F_x$  is adjusted. When the two sides are equal the solutions are valid. For these calculations  $E$  was considered to be 170 GPa.

During peeling the anchor point is not allowed to have horizontal movement. This constraint has dramatic effects on transverse-force/deflection behavior of the beam. As seen in Figure 3 the beam displays nonlinear stiffness as its height increases. The plot also shows the linear force/deflection behavior of a fix-fix beam with a small deflection assumption. The linear model deviates by more than 5% for displacements greater than  $27.07\% \approx \frac{1}{4}$  of the beam's thickness. For these experiments the beams were  $2.3 \mu\text{m}$  thick thus for an  $h > 622 \text{ nm}$  the deflection should be considered nonlinear.

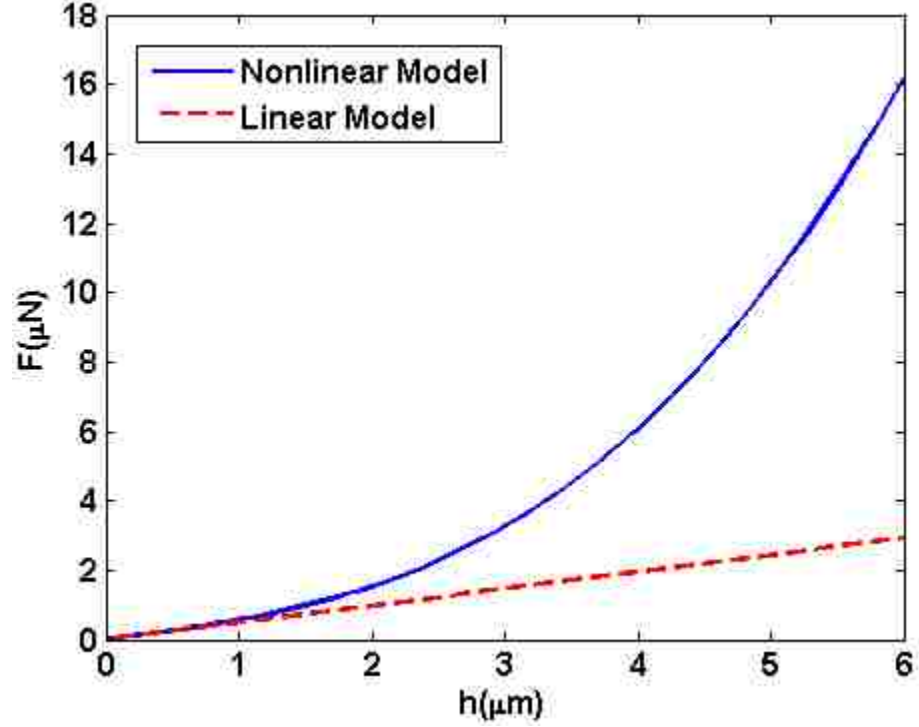


**Figure 3:** *Comparison between the linear and nonlinear model developed in this work for a fix-fix beam with ends offset by a distance  $h$*

## 2.2 Strain Energy Release Rate Formulation

Griffith's criterion predicts that a crack will propagate when the work done by the external force exceeds the summation of elastic energy stored in the beam and the energy stored in the crack tip. In the case of a stiction failed beam at rest it can be considered as have no external force applied. Thus the strain energy release rate is defined as:

$$G = -\frac{1}{w} \frac{\partial U}{\partial s} \quad (9)$$

where  $U$  and  $w$  represent the elastic energy stored in the  $\mu$ cantilever and width of the  $\mu$ cantilever, respectively. Because the crack is not propagating the strain energy release

rate must equal the crack resistance or its adhesion. Note that due to the nature of these experiments the arrested crack value is reported. When  $h$  is small the beam behaves as a linear elastic spring to a good extent, but as the beam's height increases, a nonlinear model must be utilized (see Section 2.1). In the linear case,  $U$  can be readily found by using:

$$U = \int_0^S \frac{M^2}{2EI} dx \quad (10)$$

(10) considers that the beam's strain energy is only due to bending. Had its deformed shape and strain energy only been due to bending, it would have followed the linear model in Figure 3. Clearly, for  $h > 622$  nm, the beam's behavior is not linear. Thus the nonlinear model developed in Section 2.1 more accurately models the deflection of the  $\mu$ cantilevers. In order to find the elastic strain energy associated with the nonlinear model, it is necessary to integrate the work done by each of the forces and moments acting on the beam during its entire deformation history.

The strain energy stored in the elastic silicon beam is equal to the total mechanical work done on the beam while inducing the deformation. The work done on the system can be considered to be composed of three parts, the work done by shear forces, normal forces and bending moments. Usually if the work done by the shear forces and normal forces (tensile or compressive) are ignorable compared to the work of bending moments, the total work may be calculated using (10) with acceptable accuracy. This equation is widely used to calculate the strain energy in silicon  $\mu$ cantilevers [41], [42], [44], [46], [47], [38], [50], [51].

The following work demonstrates that relatively large tensile/compressive stresses and therefore strain energies can develop during testing. Development of these forces and strain energies is dependent on the height of the anchor point  $h$ . The following section demonstrates a method for calculation stored energy. In this method the total stored energy is calculated by integrating the infinitesimal work done by each force during an infinitesimal motion of the anchor point. The other energy method developed in Mousavi, Kashamolla and Leseman [52] is used to verify the results obtained using this method. In the other energy method developed, three subsequent deformations are induced, one after the other, by applying the external transverse, longitudinal forces, and the bending moment. The two methods are found to be consistent.

In this method, the anchor point is considered to move infinitesimally up while preventing it from moving horizontally or undergoing under any kind of rotation. The magnitude of the forces and moments developed in the beam at the anchor point are calculated using (4) to (8). The strain energy is then calculated by integrating the work done by these forces and moments during the deformation as shown in (11).

$$U = \int_0^h F_y dy + \int_0^0 F_y dx + \int_0^0 M_{(x=s)} d\theta = \int_0^h F_y dy \quad (11)$$

Because the anchor point is only allowed to move vertically, it is only the transverse force  $F_y$  that leads to nonzero work. Although the bending moment and the tensile force do not do any mechanical work during each infinitesimal step but their effects are inherent in the magnitude of  $F_y$ . The result of integration is the total work done by all external forces applied on the system. Some of the external forces/moments directly

contribute to the equation and some are inherent, but all affect the total strain energy stored in the beam.

## 2.3 Mode II Theory

### 2.3.1 Theory to Determine Upper Bounds of $G_{II}$

To run the Mode II experiments we make use of a MEMS actuator on which is an attached microcantilever beam. The component that governs the motion of the actuator is stiffness of the actuator's flexure spring. Here we present the theory of actuators and equations of the flexure springs. There are various types of flexure springs that are used in MEMS actuators. The most commonly used flexure springs [53] are the fix-fix flexure, crab-leg flexure, folded flexure and serpentine flexure. The MEMS actuator used in these experiments uses a fix-fix flexure because of its high stiffness when compared to other flexures of equal dimensions. For fix-fix flexures with small deflections a linear relationship exists between the force and deflection:

$$F = k\delta \quad (12)$$

Where  $k$  is the stiffness and  $\delta$  is the displacement. When a load is  $F$  is applied at the center of the fix-fix beam then the above equation becomes [54]:

$$F = \frac{24EI}{L^3} \delta \quad (13)$$

where  $\delta$  is the deflection at the center of the beam. Design of a fix-fix flexure is shown in Figure 4.

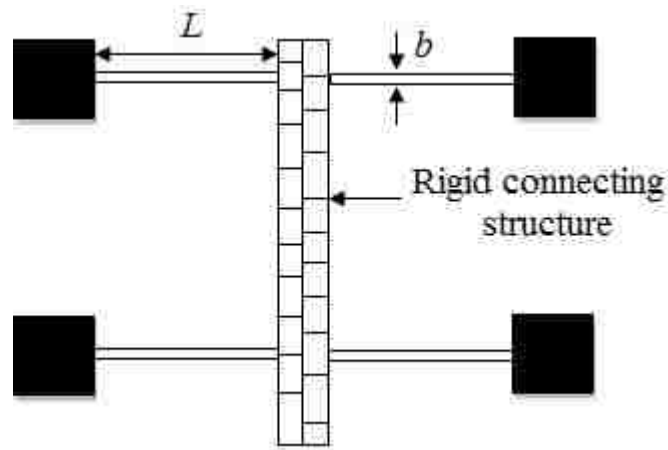


**Figure 4: Design of fix-fix flexure**

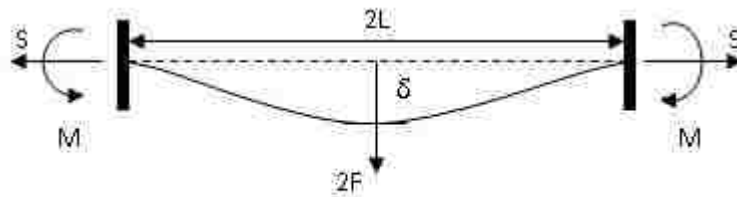


**Figure 5: Free body diagram of the fix-fix beam**

However for large displacements ( $\delta > \frac{1}{4}t$ ) the springs behave in a nonlinear fashion due to axial force that develops. Reference [49] gives the derivation for the behavior of the fix-fix beams when a load  $2F$  is applied at the center of the beam and deflection,  $\delta$ , is developed, see Figure 5. Analyzing the free body diagram and solving the resulting differential equations and compatibility conditions the following set of simultaneous equations are found.



$$\delta = 2 \left( \frac{2I}{A} \right)^{\frac{1}{2}} (u - \tanh u) \left( \frac{3}{2} - \frac{1}{2} \tanh^2 u - \frac{3 \tanh u}{2u} \right)^{-1/2} \quad (14)$$

$$F = \frac{8EI}{L^3} \left( \frac{2I}{A} \right)^{\frac{1}{2}} u^3 \left( \frac{3}{2} - \frac{1}{2} \tanh^2 u - \frac{3 \tanh u}{2u} \right)^{-\frac{1}{2}} \quad (15)$$

$$u = \sqrt{\frac{S}{EI}} \frac{L}{2} \quad (16)$$

where  $S$  is the axial force,  $A$  is the cross sectional area,  $I$  is second moment of inertia of the beam,  $2L$  is the full length of the beam and  $E$  is the Young's modulus of the beam material. By solving the above equations and by curve fitting we have a force equation developed based on the dimensions of the beams used in the actuator device. The theoretical force versus displacement curve drawn for the fix-fix flexure used in this work is shown in Figure 6. The dimensions are  $L = 245.64 \mu\text{m}$ ,  $w = 4.25 \mu\text{m}$  and  $h = 20.12 \mu\text{m}$  as verified in a SEM.

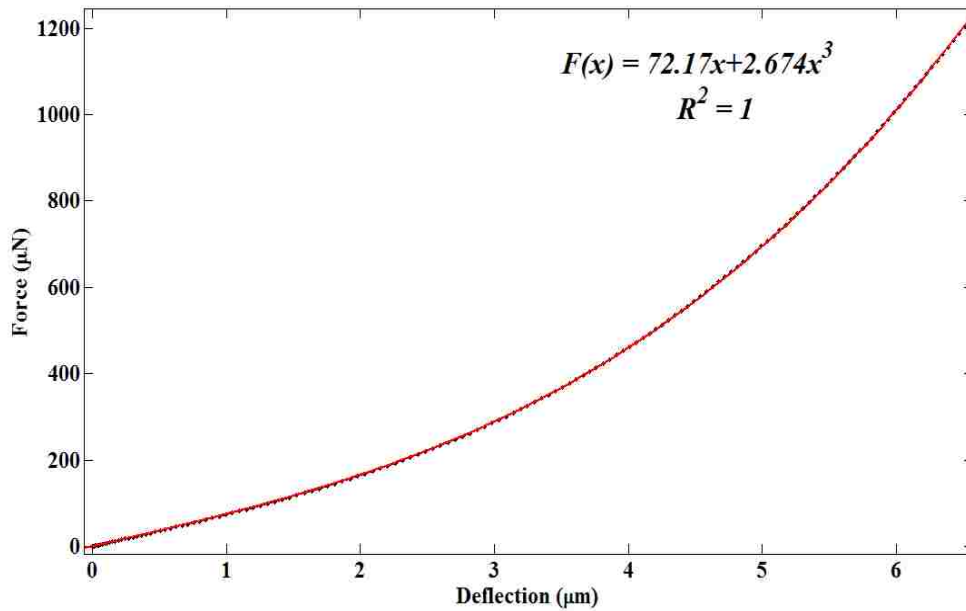


**Figure 6: Force versus deflection theoretical curve for a fix-fix beam**

(14) - (16) are quite complex, yet they produce a relationship that can be readily fit using a linear and a cubic term. Specifically,  $F = ax + bx^3$  where  $a$  and  $b$  are constants obtained from fitting. Using this form for fitting Figure 6 and the like can be typically fit with  $R^2$  values better than 0.99.

The fix-fix flexure applies the force to a microcantilever beam that has been attached to the shuttle of the fix-fix flexure. The force is transmitted through the microcantilever beam to a substrate on which the microcantilever beam is stiction failed. The microcantilever therefore acts like as a tensile member when transmitting the load. Loading of the stiction failed cantilever beam is shown in Figure 7. Note that the microcantilever beam is attached after fabrication of the fix-fix flexure and its shuttle.

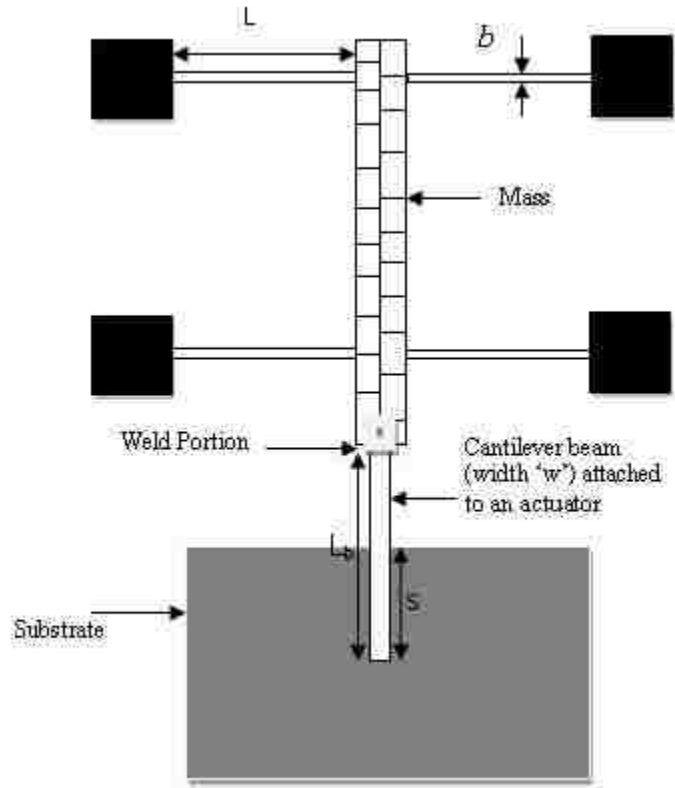


**Figure 7: Design of fix-fix beam flexure with cantilever beam attached**

Consider the tensile forces acting on a cantilever beam as shown in Figure 8. The elastic strain energy  $U$  stored in this cantilever beam is given by (17):

$$U = \frac{F^2(L_b - s)}{2EA} \quad (17)$$

where  $F$  is the tensile load acting on the beam (from the actuator),  $E$  is the elastic modulus of the material and  $A$  is the cross sectional area of the cantilever beam.  $L_b - s$  is the free length of the beam not stiction failed on the substrate, see Figure 7.

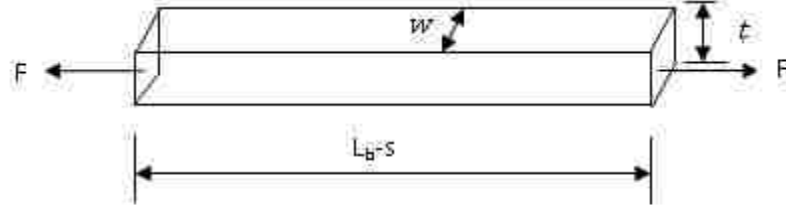


**Figure 8: Tensile beam with dimensions**

When the ‘crack’ between the cantilever and substrate is formed a new surface is created. With this configuration the crack grows uncontrollably and thus propagates until the end of the beam. The new surface has a length  $s$  and width  $w$ . These dimensions are multiplied to give the area of the new surface and then multiplying that area by the critical strain energy release rate yields the energy released to making the new surface. Equating this energy to (17) yields:

$$G = \frac{F^2}{2w^2tEs} (L_b - s) \quad (18)$$

where  $t$  is the thickness of the cantilever. Thus, the strain energy release rates from Mode II type failures at the time of crack initiation can be obtained by using the (18). (18) gives the upper bounds of the strain energy release rates, because the ‘crack’ grows beyond the free end of beam and does not terminate in the interface. In order to accurately determine the value of  $G_{II}$  an infinitesimal crack should be grown at the interface.

### 2.3.2 Theory to Determine the Exact Value of $G_{II}$

Consider the tensile forces acting on a cantilever beam as shown in Figure 9. If the cantilever beam attached to the actuator has dimensions of length,  $L$ , and width,  $w$  and thickness,  $t$ ,

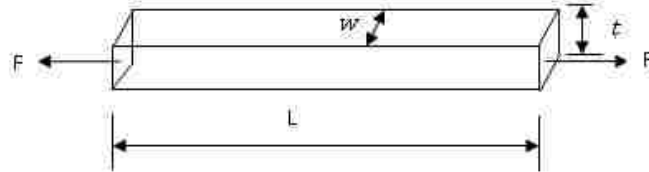


*Figure 9: Tensile beam with a length  $L$ , width  $w$  and thickness  $t$*

then the elastic strain energy  $U$  stored in a tensile member is given by (19):

$$U = \frac{F^2 L}{2EA} \quad (19)$$

where  $F$  is the tensile load acting on the beam,  $E$  is the elastic modulus of the material and  $A$  is the cross sectional area of the cantilever beam. The spring constant,  $k$ , of the tensile member is given by

$$k = \frac{EA}{L} \quad (20)$$

And the compliance,  $\lambda(L)$  of the system is given by

$$\lambda(L) = \frac{1}{k} = \frac{L}{EA} \quad (21)$$

Combining (19) and (21), we can write strain energy as

$$U = \frac{1}{2} F^2 \lambda(L) \quad (22)$$

From [46] and [55] the crack driving force is the strain energy release rate,  $G$ , for microstructure adhesion can be written as (23):

$$G = -\frac{1}{w} \frac{dU}{dL} \quad (23)$$

where  $U$  is the strain energy,  $w$  is the width of the cantilever and  $L$  is the length of the cantilever. Differentiating (22) with respect to  $L$ , we obtain

$$\frac{dU}{dL} = \frac{1}{2} F^2 \frac{d\lambda}{dL} \quad (24)$$

If crack propagation occurs with work done by load,  $F$ , combining (23) and (24) results in a strain energy release rate given by (25):

$$G = \frac{1}{2} \frac{F^2}{Ew^2t} \quad (25)$$

where  $F$  is the load acting on the actuator. Thus, the strain energy release rates from Mode II type failures can be obtained by using the (25).

## CHAPTER 3

### EXPERIMENTAL SETUP

#### 3.1 Experimental Setup for Mode I and Mode II

The proposed experimental setup is capable of measuring the Mode I, Mode II and Mode III interfacial adhesion energies of MEMS devices failed on the substrate. The concept for these experiments is based on the peel test as developed for microcantilevers by Leseman *et al.* [46], [47]. At the core of the setup is a freestanding  $\mu$ cantilever beam that is stiction failed onto an independent substrate (see Figure 10). By moving the base of the stiction failed  $\mu$ cantilever in the  $y$ -direction, critical strain energy release rates can be determined. Because the  $\mu$ cantilevers and the substrate on which they are to be failed on are independent from one another, it is necessary to accurately orient the  $\mu$ cantilevers to the substrate. Thus multiple rotational and translational stages are necessary.

A total of 8 degrees of freedom (DOF) are necessary to align a set of  $\mu$ cantilever to the substrate on which they are to be stiction failed; 2 DOF's are rotational and 6 are translational. A picture of the final setup is shown in Figure 10. The stages that facilitate the 8 DOF are grouped into two sets of stages, 'Group A' and 'Group B'. Group A control the position and orientation of the  $\mu$ cantilevers while Group B control the position and orientation of the substrate. The handle in the rear of the Group A stages (Figure 10) controls  $y$ -axis motion and the large black stage is a piezoelectric stage with  $x$ ,  $y$ , and  $z$  motion capabilities. Connected to the black piezoelectric stage is a rigid macro-cantilever with a T-shaped cross section. This cantilever has the  $\mu$ cantilevers attached to it, at its free end, (see inset of Figure 10). The substrate that lies under the  $\mu$ cantilevers in the inset of Figure 10 is attached to translation stages that move in the  $x$ - $z$  plane. Stacked on



top of these translational stages, are two rotational stages that pivot around axes parallel to the x and z axes.

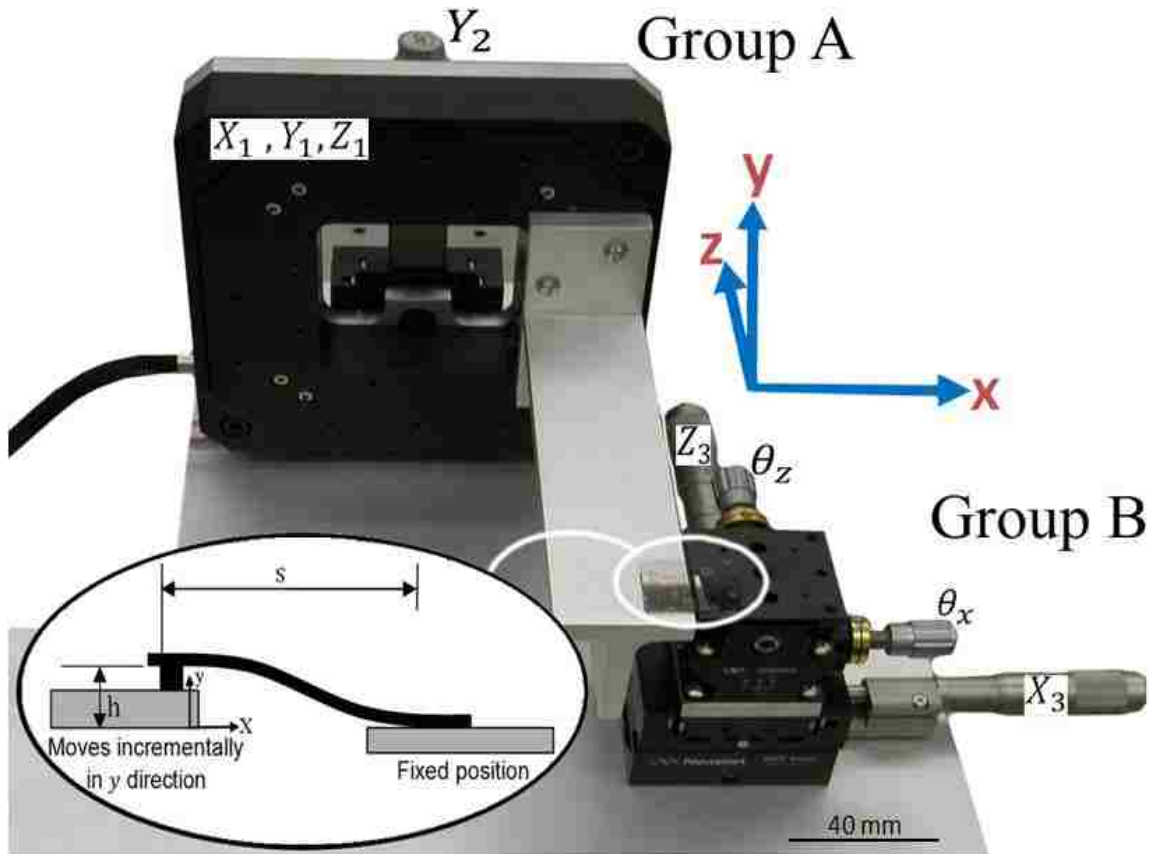


**Figure 10:** *Experimental setup showing the apparatus for measuring Mode I and Mixed Mode adhesion energies*

All 6 translational DOF's are orthogonal to one another with 3 being redundant. Though the direction of translation is redundant the resolution is not. All translational stages with handles in the setup have 1  $\mu\text{m}$  resolution while the piezoelectric stages all have better than 1 nm of resolution. The range of motion for the piezoelectric stages are 200  $\mu\text{m}$ , 200

$\mu\text{m}$ , and  $20 \mu\text{m}$  for the x, z, and y axes respectively. The rotational axes have  $8 \text{ sec} \approx 0.0022^0$  of resolution.

In order to determine the  $y(x)$  profiles of the  $\mu$ cantilevers as they are peeled from the substrate, a vertical scanning interferometer is employed which has 3 nm of displacement resolution. A custom baseplate was machined for mounting both of the groups of stages underneath the interferometer. The stages are offset from the center of the baseplate because of the physical envelope of the interferometer not allowing for insertion of the piezoelectric stage under it. The remedy for this spatial issue was the T-shaped cantilever.

For these experiments the  $\mu$ cantilever beams used were fabricated at Sandia National Laboratories using the Sandia Ultra-planar, Multi-level MEMS Technology 5 (SUMMiT V<sup>TM</sup>). This process uses a specific set of fabrication processes to make MEMS devices by surface micromachining using as many as fifteen masks [56]. The structural material is Poly-Si deposited by LPCVD. The sacrificial material is  $\text{SiO}_2$ , also deposited by LPCVD. Other parts of the process sequence include plasma etches (RIE) for small parts of the devices and a wet etch for certain parts (hubs). The final release step is a wet etch using HF acid. SUMMiT V uses 5 levels of Poly-Si layers (Poly0, Poly1, Poly2, Poly3, and Poly4) and sacrificial oxide layers (Sacox1, Sacox2, Sacox3 and Sacox4) & 14 photolithography steps. The Poly0 layer is attached to the substrate, while the main structural layers are a laminate of Poly1, Poly2 (called Poly12), Poly3 and Poly4. Poly0 layer is used for electrical interconnect and as a ground plane. Poly1 to Poly4 are the mechanical construction layers. At the end, it has 1 ground plane and 1 electrical layer with 4 mechanical layers. Devices up to  $12 \mu\text{m}$  high with large stiffness and robustness

can be made by using this process. A schematic of the lay-up for films is shown in Figure 11.

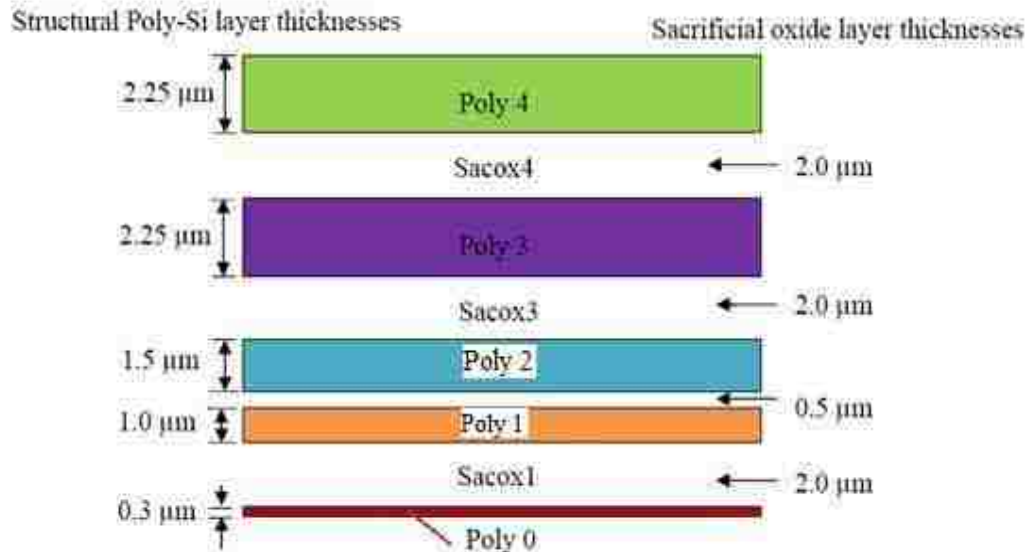


**Figure 11: The physical layout of SUMMiT V™ Material Layers with 5 levels of poly-Si and 4 layers of sacrificial oxides**

The left side of the figure denotes the thicknesses of the poly-Si layers deposited and the right side dimensions are the thicknesses of the sacrificial oxides deposited. These dimensions are the nominal values and according to [57] they are prone to  $\pm 10\%$  tolerance. The specific  $\mu$ cantilevers used in this process consist of the Poly-1 and Poly-2 layers without a layer of sacrificial oxide between them.  $\mu$ cantilevers used in this work were 1500  $\mu\text{m}$  and 1000  $\mu\text{m}$  long, 30  $\mu\text{m}$  wide and 2.3  $\mu\text{m}$  thick. SUMMiT  $\mu$ cantilevers were chosen due to the amount of work previously done in characterizing the critical strain energy release rate of structures created with this process [46], [38], [47], [44], [56], [10], [45], [50]. In the discussion section of this thesis results using  $\mu$ cantilevers and

different characterization techniques are compared and contrasted.

Arrays of released  $\mu$ cantilevers are received from Sandia National Labs with substrates under the extents of the  $\mu$ cantilevers. In order to perform the peel tests the substrates need to be removed from under the free length of the  $\mu$ cantilevers. This is accomplished by scribing the substrate perpendicular to the length of the beam near their base on opposing sides. Scribing, in this case, is performed using a Nd:YAG laser cutting system. Then, with the  $\mu$ cantilevers on top, the portion of the substrate under the  $\mu$ cantilever beams is extended off the end of a glass slide such that the scribe marks are in-line with the edge of the glass slide. The die is held rigidly behind the base of the  $\mu$ cantilevers and a load is applied at the end of the substrate beyond the end of the  $\mu$ cantilevers. This load and moment cause a crack to propagate between the scribe marks on either side of the  $\mu$ cantilevers. The amount of substrate remaining under the free length of the beams is no more than 7  $\mu\text{m}$  in length. This method produces no noticeable debris on or around the microcantilevers. All experiments were conducted in a cleanroom environment. Experiments were conducted at an average temperature of 70.2  $^{\circ}\text{F}$  and relative humidity was controlled to 36% all at an approximate pressure of 625 *Torr*.

## CHAPTER 4

### EXPERIMENTAL PROCEDURE

#### 4.1 Experimental Concept and Procedure for Mode I

The experimental procedure can be broken into three main steps. First the experimental apparatus (Figure 10), is mounted onto and aligned to the interferometer. Second, the  $\mu$ cantilevers are stiction failed onto the substrate. Third, the base of the  $\mu$ cantilever beams are raised above the substrate, onto which they are stiction failed, and the  $\mu$ cantilevers' out-of-plane deformations are measured. Using the crack lengths, which are measured by postprocessing the  $\mu$ cantilevers' deformation data, the strain energy release rates can be determined. A schematic representation of Mode I experiments is shown in Figure 12.

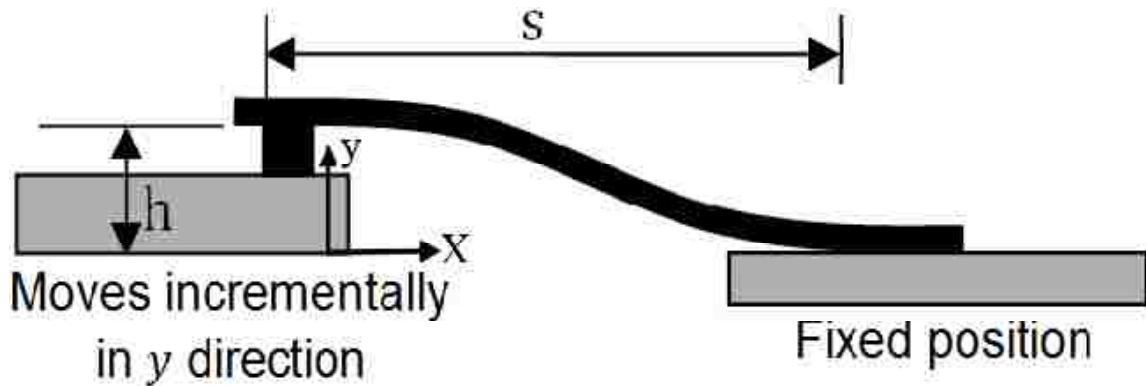


*Figure 12: Schematic representation of experiments for Mode I*

Mounting and alignment of the experimental apparatus is multi-step process. For mounting, the baseplate shown in Figure 10 is attached to the translational stage of the interferometer which is parallel to the x-z plane of the apparatus. Alignment of the

$\mu$ cantilevers and substrate to the interferometer is the next step. With the free ends of the  $\mu$ cantilevers positioned above the substrate onto which they will be failed, the head of the interferometer is adjusted using stages that rotate about the x and z axes. Once the  $\mu$ cantilevers are parallel to the interferometer, the substrate is brought into focus. In order to make the substrate parallel to the interferometer the goniometers from the Group B stages are adjusted. At this point the substrate is parallel to the interferometer and so are the  $\mu$ cantilevers. Therefore the substrate and  $\mu$ cantilevers are parallel to one another as well.

With the  $\mu$ cantilevers and substrate parallel to one another, the  $\mu$ cantilevers are stiction failed on the substrate. This is accomplished by lowering the  $\mu$ cantilevers using the Group A stages. The coarse stages are used for the initial approach and the piezo stages are used when the cantilevers are within approximately 10  $\mu\text{m}$  of the substrate. The top-view of the microcantilever beams placed above the substrate is shown in Figure 13.  $\mu$ cantilevers are positioned 2 - 3  $\mu\text{m}$  above the substrate and then a drop of isopropyl alcohol (IPA) is placed on top of the  $\mu$ cantilever / substrate combination to induce stiction failure.

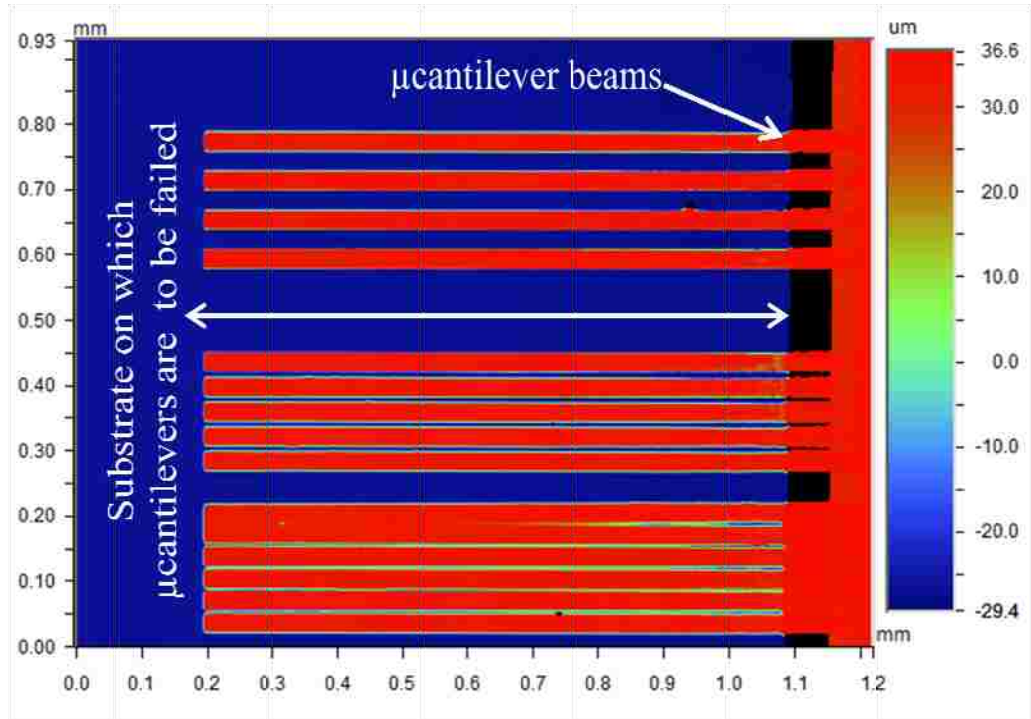


**Figure 13: Top-view of the microcantilever beams placed above the substrate**

After the liquid used to stiction fail the  $\mu$ cantilevers has completely evaporated, the bases of the  $\mu$ cantilevers are raised in order to peel the stiction failed portion of the  $\mu$ cantilevers from the substrate. Using the y-axis of the piezo stage of Group A, the bases of the  $\mu$ cantilevers are indexed in the positive y-direction in 100 nm increments. At each increment an inteferometric image of the  $\mu$ cantilever beam array is captured. These images contain the complete 3D information about the profile of each  $\mu$ cantilever. Postprocessing of these images can be used to reconstruct the 3D profile of these  $\mu$ cantilevers (see Figure 14). Typically, more than 700 data points are captured for a single beam's deflection profile resulting in an out-of-plane measurement accuracy of 3 nm. This data is later used to calculate the strain energy release rates of the beams as described in the subsequent sections.

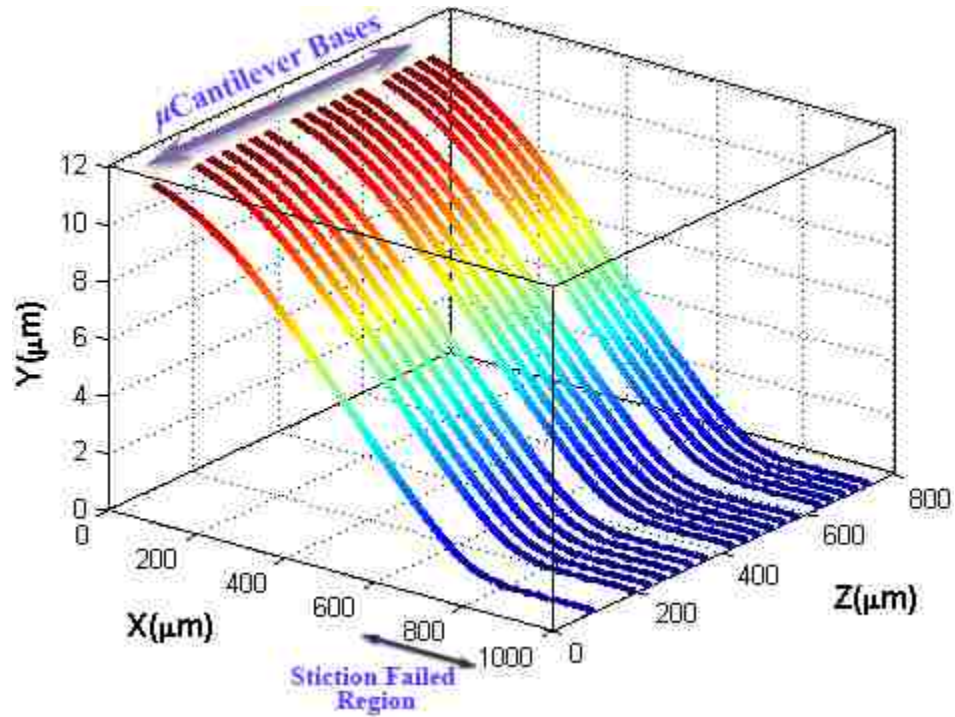


**Figure 14:** *3D profile of 1000μm length cantilever beams stiction failed in an s-shaped profile*

#### **4.2 Experimental Procedure for Mode II**

The proposed experimental method for measuring the Mode II interfacial adhesion energies for stiction failed MEMS devices uses a microcantilever beam (1500 μm long, 30 μm wide and 2.3 μm thick) attached to MEMS actuator with fix-fix beams flexure. Deflection of the spring is measured with the vernier scale of the actuator. Then a nonlinear elastic model of the fix–fix beam flexure is used to determine the interfacial adhesion energy between the failed microcantilever beam and the surface, see the Section 2.3



#### 4.2.1 Microcantilever Beams Fabrication

In these experiments we used microcantilever beams fabricated at Sandia National Laboratories using the SUMMiT V<sup>TM</sup> process which is to be ‘welded’ to MEMS actuator using a focused ion beam (FIB) with a gas injection system (GIS). The details of the microcantilevers fabrication are discussed earlier in experimental setup Section 3.1 in more detail. A set of exemplary microcantilever beams is shown in Figure 15. Beams are to be attached to the MEMS device using a FIB system as described in the subsequent section. These beams are to be failed on an independent substrate and a tensile force along the longitudinal axis of the beam will be applied causing a sliding (Mode II) failure of the beam. Note that this method is general and other surfaces could be attached to the MEMS actuator that applies the force. However, several researchers, including the present author, have used SUMMiT V beams for Mode I failures and thus it was desired to be able to correlate this data with previous data.

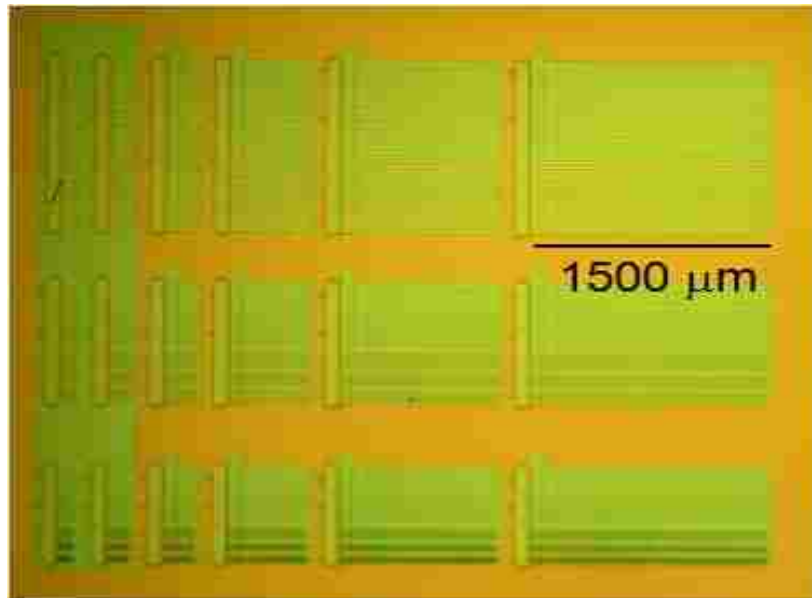


**Figure 15:** *Top view of microcantilever beams fabricated with the SUMMiT V<sup>TM</sup> process*

#### **4.2.2 MEMS Actuator Fabrication**

The fabrication process followed to make the MEMS actuator is detailed out in references [58] and [53], the following is a brief discussion of the process. A Silicon on Insulator (SOI) wafer whose device layer was 20  $\mu\text{m}$ , buried oxide (BOX) 1  $\mu\text{m}$  and the handle layer was 600  $\mu\text{m}$  thick was utilized. The device layer and handle layer are p-type doped with boron and all crystal orientations were (100). A single mask process was used to transfer the pattern of actuator into a photoresist layer. The device layer was then etched to the BOX layer by deep reactive ion etching (DRIE) of Si, using the Bosch Process [59]. This process creates high aspect ratio structures by etching nearly vertically from the edge of the PR layer. Next, the PR layer is removed using acetone, isopropyl alcohol, and deionized (DI) water rinses respectively. An oxygen ( $\text{O}_2$ ) plasma is used to remove any small remaining amount of PR on the Si surface. Finally, the actuator is released by etching the BOX layer in HF bath and then rinsed in DI water. Once the etching has completed, the device is placed on the hot plate for a few minutes in order to evaporate any remaining water. Once the device is tested and found to be moving freely then it is taken to the FIB machine to weld the microcantilever beam to the device. The fabricated actuator device is shown in Figure 16. The procedure for welding the microcantilever beam to the MEMS actuator device is described presently.

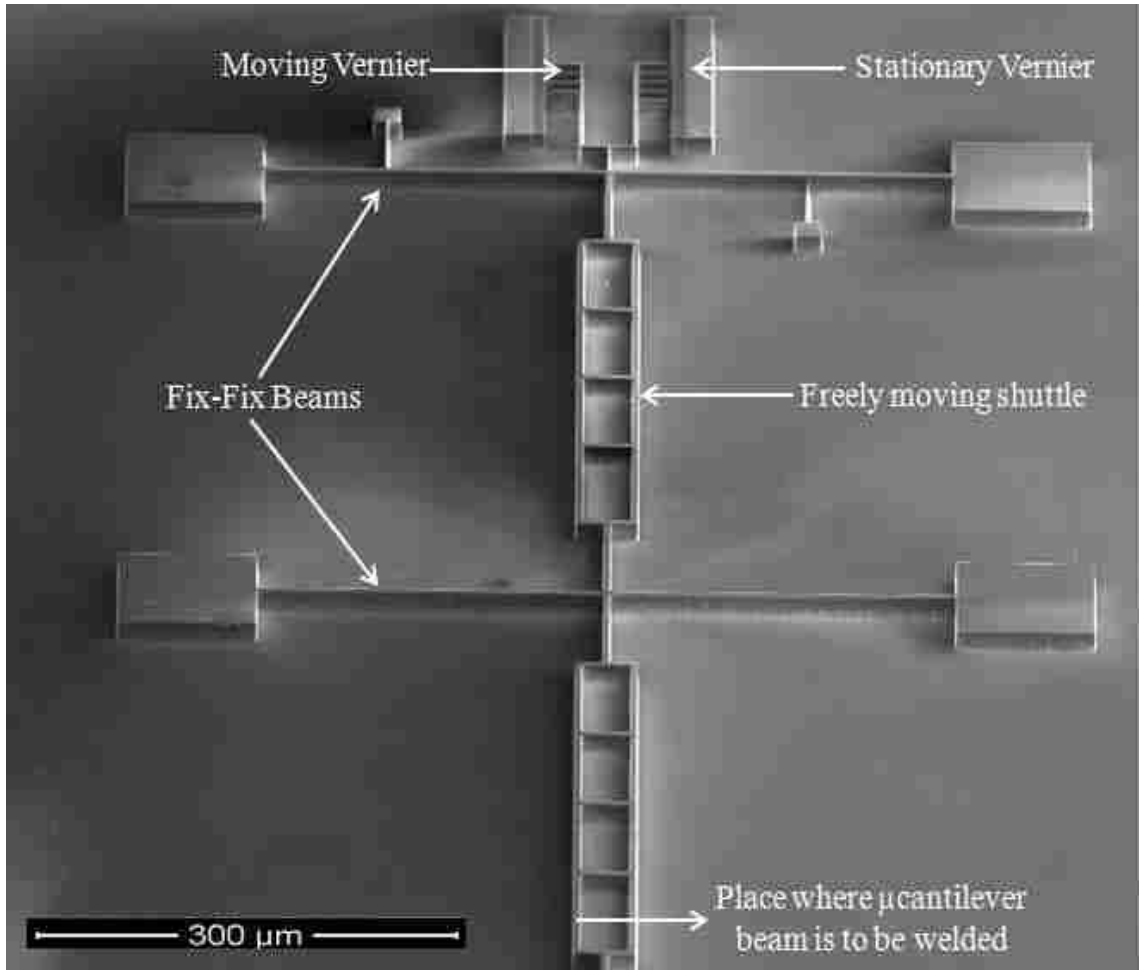


**Figure 16:** *SEM image of the MEMS Actuator device fabricated for Mode II experiments*

#### **4.2.3 Experimental Device preparation**

To prepare an experimental device to carry out Mode II experiments we used a Quanta 3D FEG, which integrates a Scanning Electron Microscope (SEM) and Focused Ion Beam (FIB). An Omniprobe and gas injection system (GIS) are utilized in order to transfer the microcantilevered beam fabricated in the SUMMiT process to the MEMS actuator that was custom fabricated, per the previous section.

An image of microcantilever beams used is shown in Figure 17. An image of the Omniprobe attached to the microcantilever and the microcantilever is cut loose at the base in order to transfer the microcantilever beam onto the moving shuttle of the MEMS actuator is shown in Figure 18. Transfer of microcantilever beam to the freely moving shuttle is shown in Figure 19. Microcantilevers are ‘welded’ onto the MEMS actuator using Pt metal straps as seen in Figure 20. The MEMS actuator with SUMMiT V microcantilever welded to it is shown in Figure 21. The right hand side of the cantilever is has no substrate underneath it. This end will be stiction failed on a substrate and then the MEMS actuator’s die is to be indexed back using a piezo-stage to applied forces to the interface between the microcantilever beam and substrate. The dimensions of the actuator used for the experiment is shown in Figure 22.

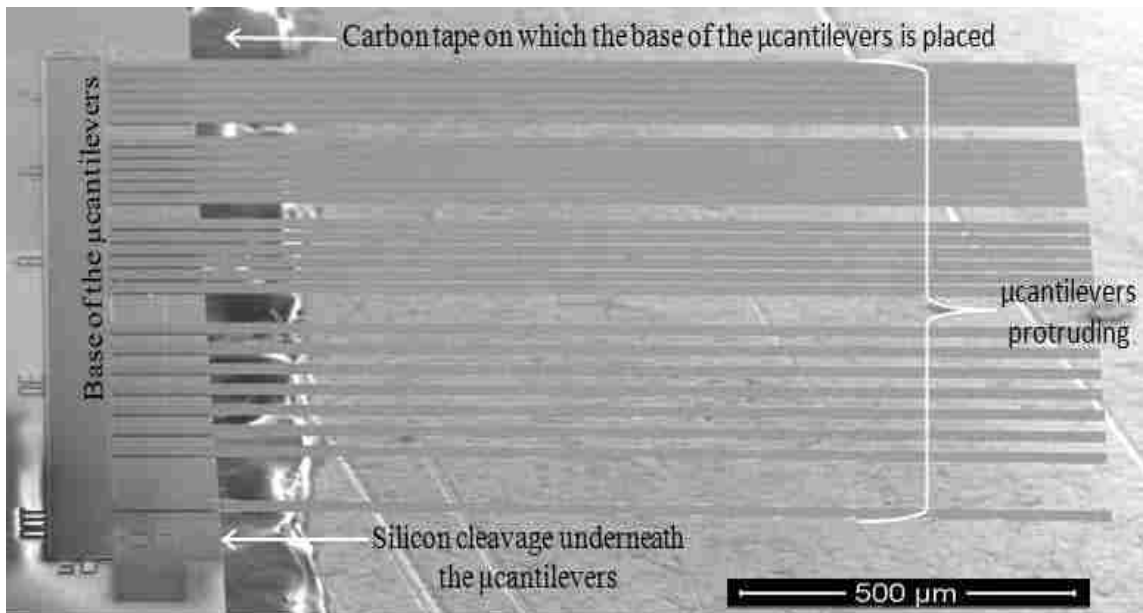


**Figure 17: SEM image of the  $\mu$ cantilever beams used for experimental device preparation**

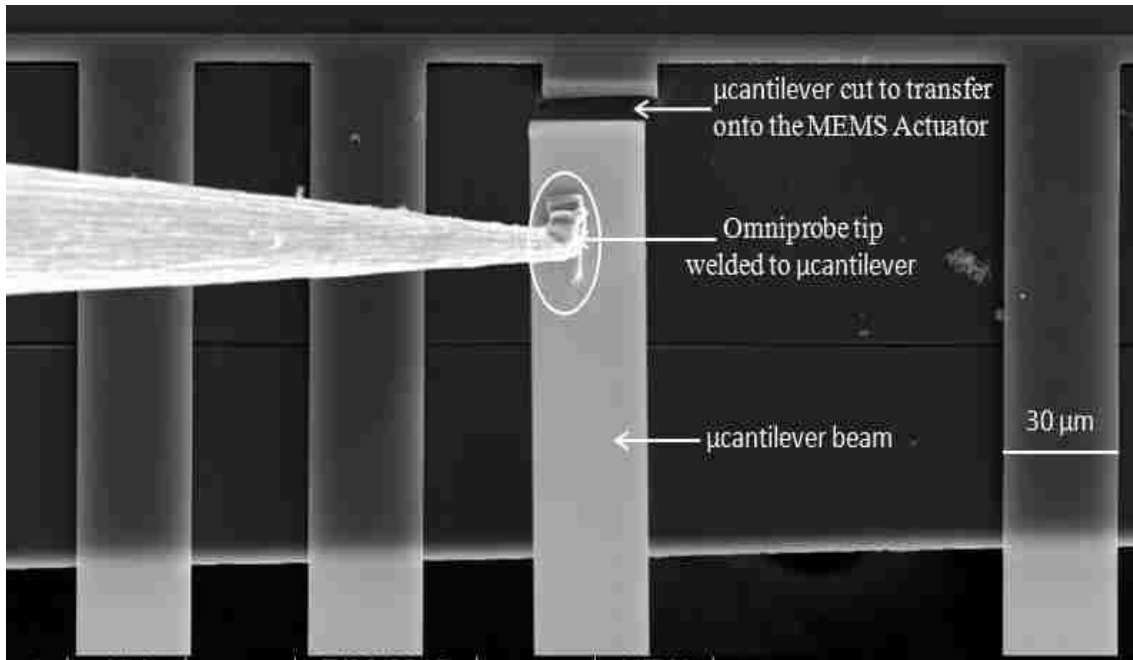


**Figure 18:** SEM image of the omniprobe welded to the  $\mu$ cantilever beam and is cut loose to transfer onto the MEMS Actuator

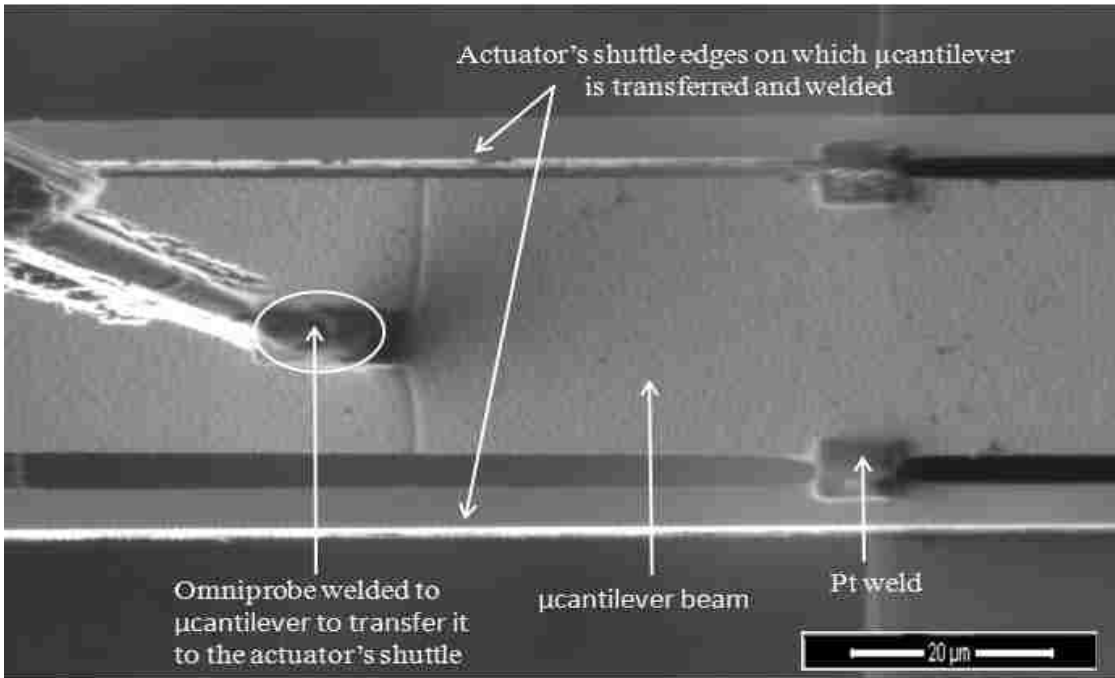


**Figure 19:** SEM image of the omniprobe transferring the  $\mu$ cantilever beam onto the freely moving shuttle of the MEMS Actuator

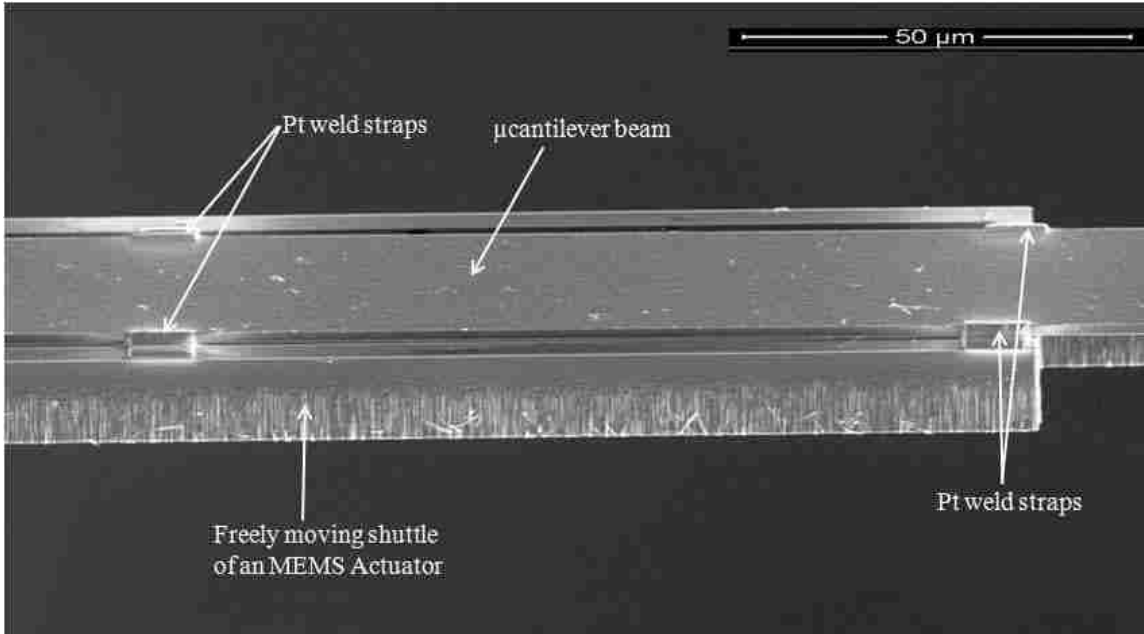


**Figure 20:** SEM image of the  $\mu$ cantilever beam welded on the freely moving shuttle of an MEMS Actuator (Pt straps used to weld  $\mu$ cantilever and shuttle are seen)

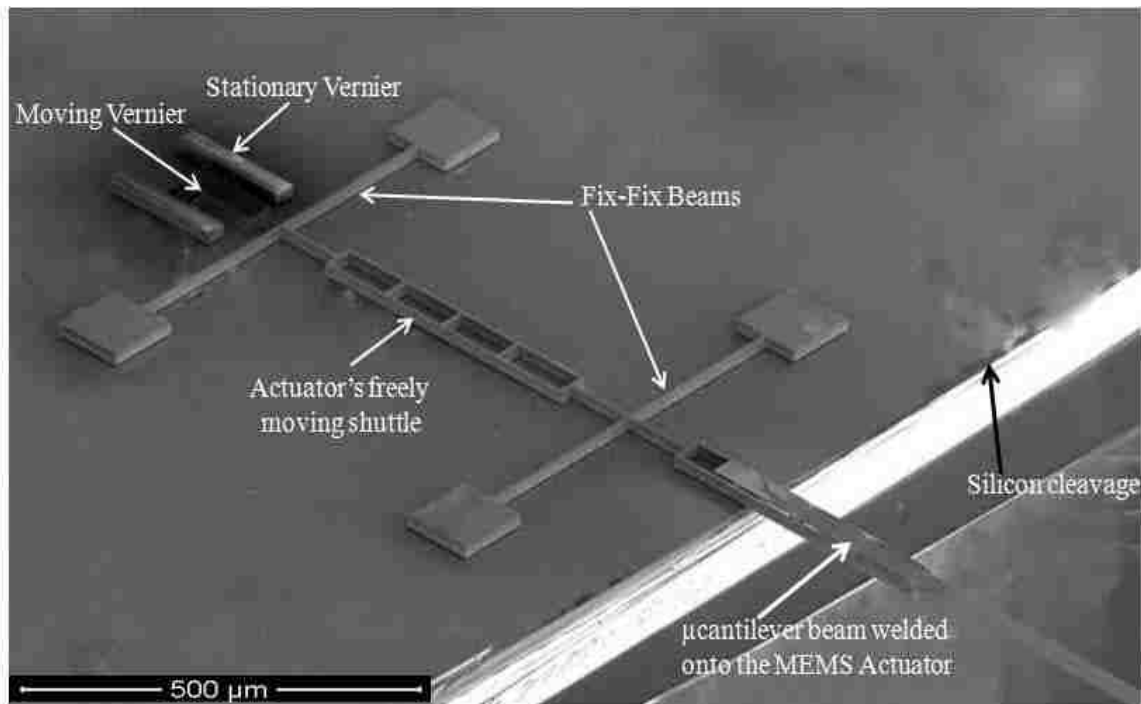


**Figure 21:** SEM image of a Mode II experimental device with a  $\mu$ cantilever beam welded to the MEMS Actuator

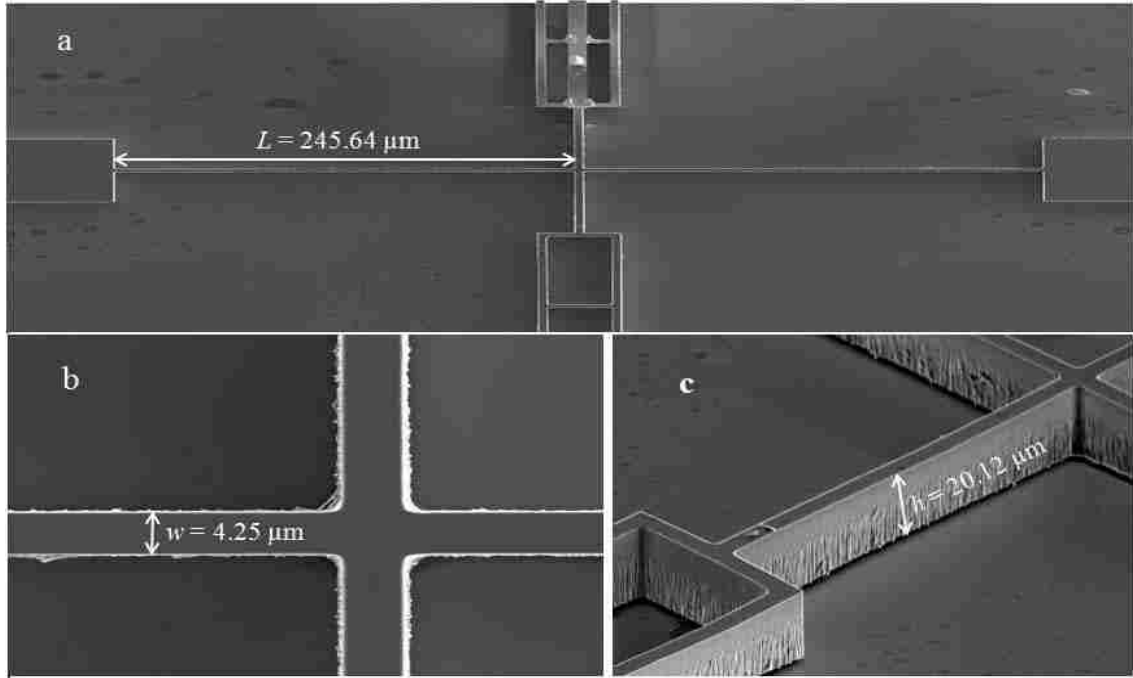


**Figure 22:** SEM image of an actuator dimensions a) length of the beam b) width of the beam c) height of the beam

### 4.3 Experimental Concept for Mode II

#### 4.3.1 Experimental Concept to Determine Upper Bounds of $G_{II}$

The same experimental setup discussed earlier in Chapter 3 is used to carryout Mode II experiments. Experiments are performed under the scanning interferometric microscope which can measure the displacement of the MEMS actuator with 200 nm resolution and the profile of the  $\mu$ cantilever with 1 nm resolution. The microcantilever beam, previously attached to MEMS actuator, is aligned parallel to the interferometric microscope using the tilt of the microscopic head. The polysilicon substrate is then aligned parallel to the microcantilever beam attached to MEMS actuator using two goniometers as shown in Figure 23. Top portion of the Figure 23 is shown with the portion of the microcantilever beam that is stiction failed on the substrate and spring design. At this point the substrate

that the microcantilever is to stiction failed onto and the microcantilever beam itself are parallel to one another. The parallel alignment of microcantilever beam with respect to substrate on which it is stiction failed is done in a similar fashion as explained in detail earlier in Section 4.1. The microcantilever is placed such that it overlaps about  $155\ \mu\text{m}$  of the substrate as is shown in Figure 24. The free length of the beam, not welded or stiction failed, is  $1146\ \mu\text{m}$ .

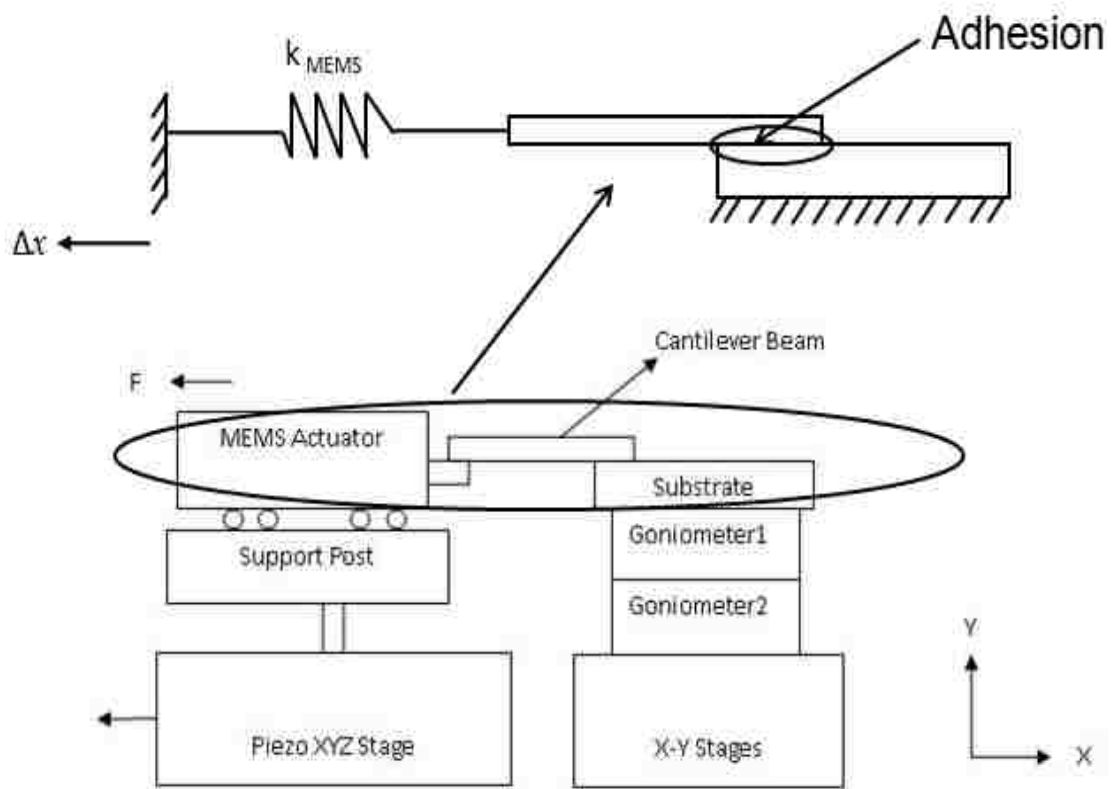


**Figure 23: Schematic representation of experiments for Mode II**



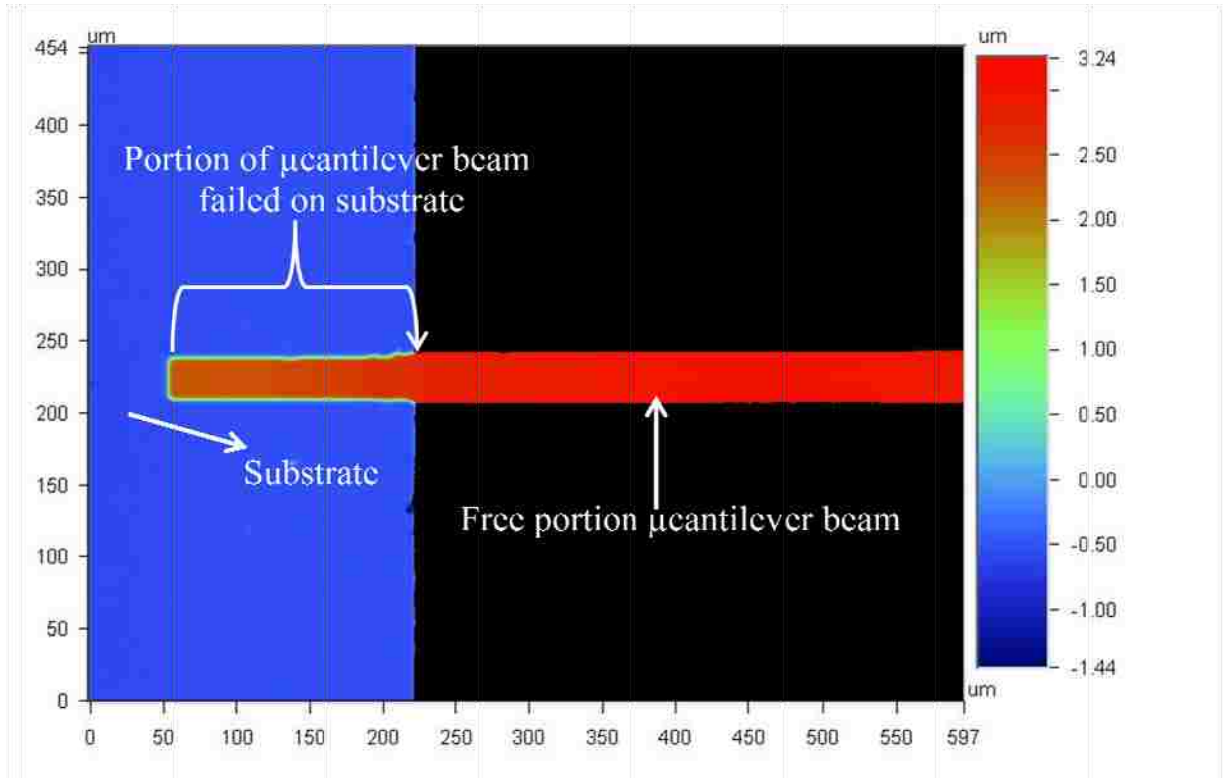


**Figure 24:** *Cantilever beam attached to MEMS actuator with fix-fix beams flexure overlapped with the substrate*

Once the alignment is made the experimental setup is not disturbed. Only the piezo actuator, which is controlled by an electronics, is moved. Next the microcantilever beam is lowered to within 2-3  $\mu\text{m}$  of the substrate then a drop of liquid DI water was then placed on the substrate, which is drawn into the gap between the microcantilever beam and the substrate by capillary forces. As the water dries, capillary forces pull the microcantilever beam into contact with the substrate overall length 155  $\mu\text{m}$  of the microcantilever beam attached to MEMS actuator. After the water has dried, the microcantilever beam is lowered with the help of piezotranslator stage (see Figure 10, Group A) such that the bottom surface of the entire microcantilever is on the same plane as the substrate on which the  $\mu\text{cantilever}$  is failed. The MEMS actuator is then pulled in

the  $-x$  direction in 250 nm increments using the piezotranslator stage. The spring displacement from the vernier scale of the actuator is noted along with the piezo displacement. The vernier scale of the actuator is shown in Figure 25. Thus knowing the stiffness and the spring displacement, the force applied to the microcantilever is calculated. This force is used to obtain the force of static friction, the kinetic friction, and also the strain energy release rate.

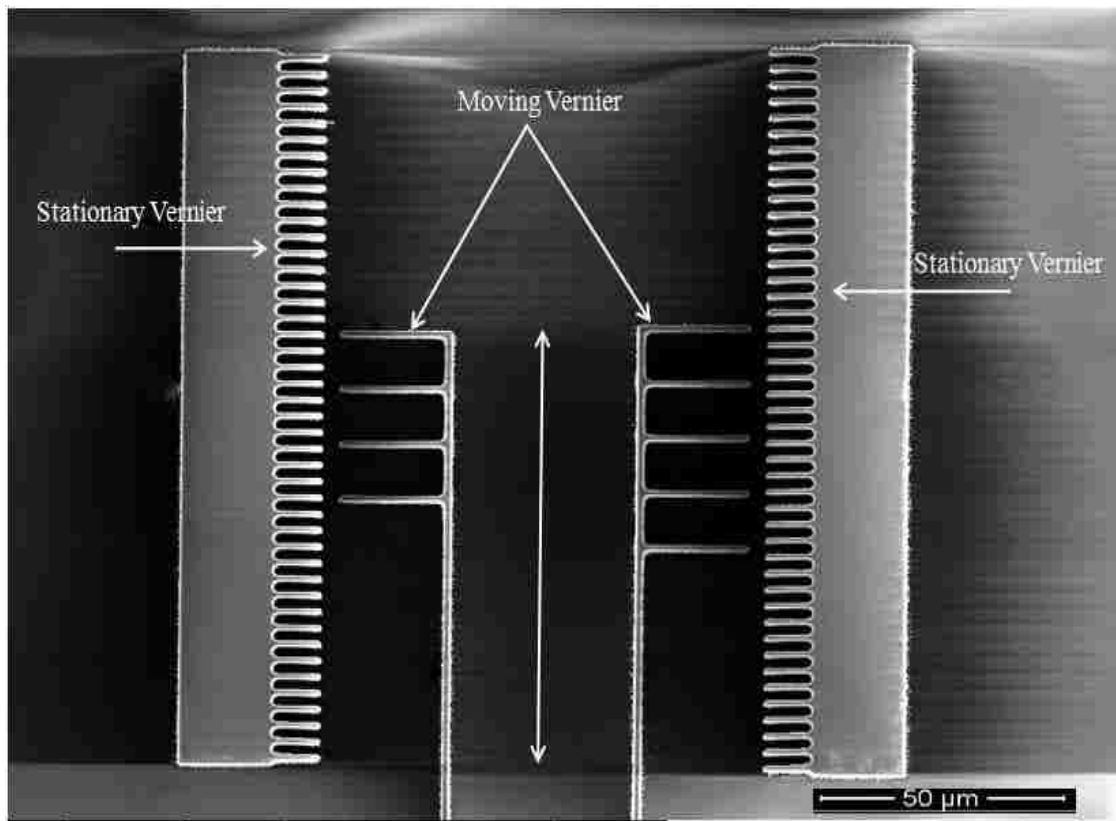


**Figure 25:** SEM image of the vernier scale of the MEMS actuator

#### 4.3.2 Experimental Concept to Determine Exact Value of $G_{II}$

From the above experiments we get the upper bounds for  $G$  values. In order to see the onset of crack growth, we performed the experiment with a small change in the procedure. The height at the base of the cantilever is raised below the 1/4 of the thickness

of the beam in order to keep the beams response linear, and the experiment is continued in the same way as described Section 4.3.1. The schematic of the experimental setup is shown in Figure 26.

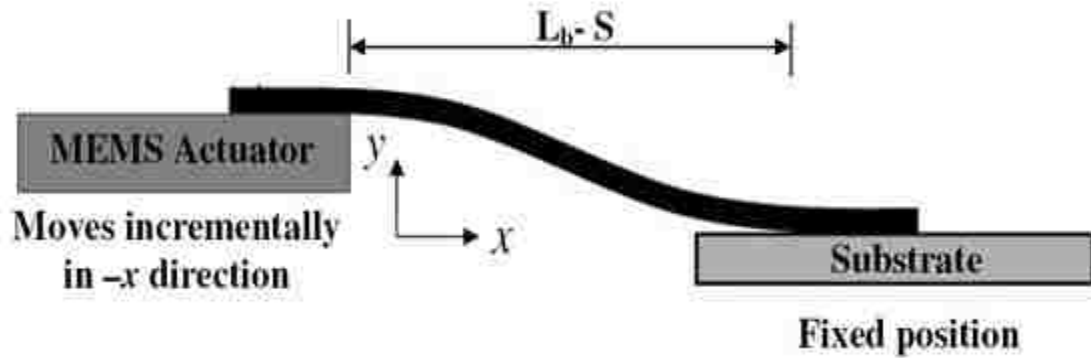


**Figure 26: Schematic representation of Mode II experiments to see the infinitesimal crack growth**

During the experiment, the microcantilever base attached to the MEMS actuator's freely moving shuttle is raised to 525 nm (see Figure 27,  $h = 525$  nm) which is less than 1/4 of micro cantilever beam thickness.

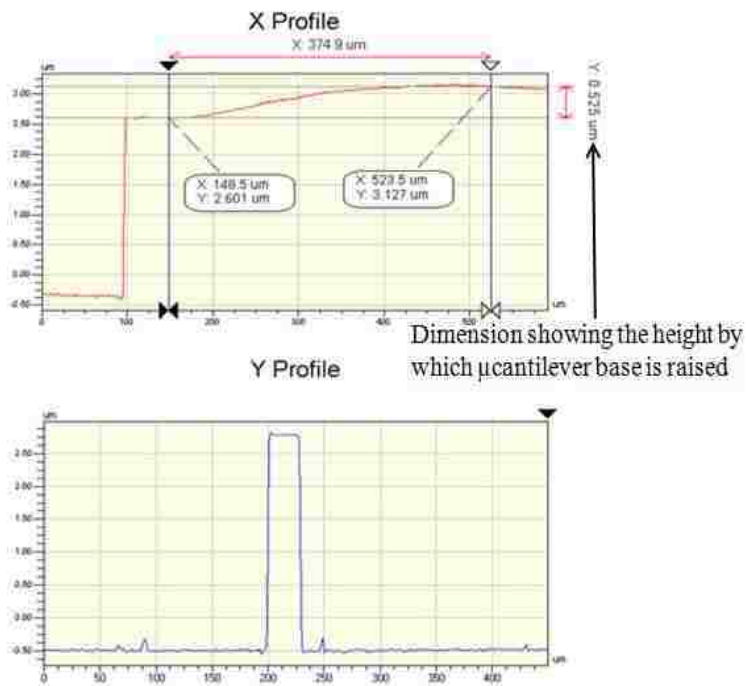
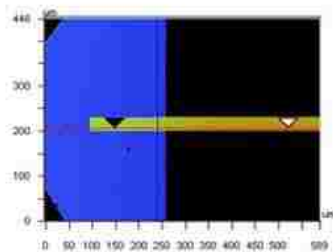


**Figure 27:** *Interferometric image showing the cantilever beam raised to  $< 1/4$  of beam thickness at the base*

## CHAPTER 5

### EXPERIMENTAL RESULTS AND DISCUSSION

#### 5.1 Experimental Results for Mode I

A set of 27 microcantilevers with lengths of 1000  $\mu\text{m}$  are used for these experiments. After raising the fixed end of the beam height in 100 nm increments as mentioned in the experimental procedure, the interferometric data is recorded and exported to fit the nonlinear model. Using the method described in Section 2.1, the data collected for this work was analyzed. For all values of  $h$ , the nonlinear model fits the data better. Specifically, the rate of root mean square (RMS) error for the linear model increases at a rate more than double that of the nonlinear model. An example of the type of fit attained is shown in Figure 28.

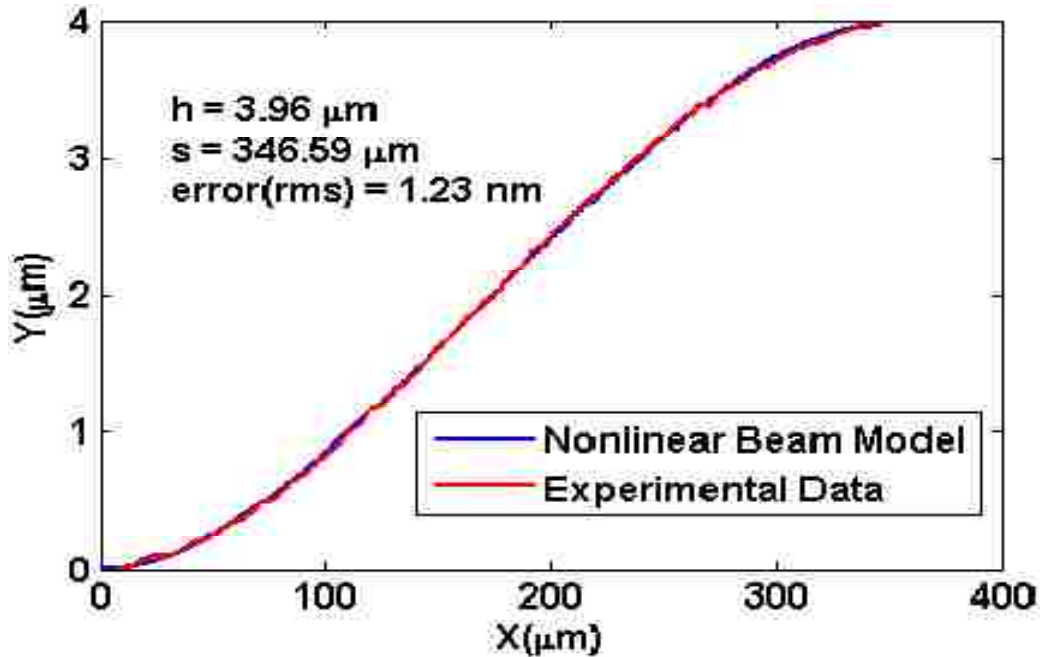
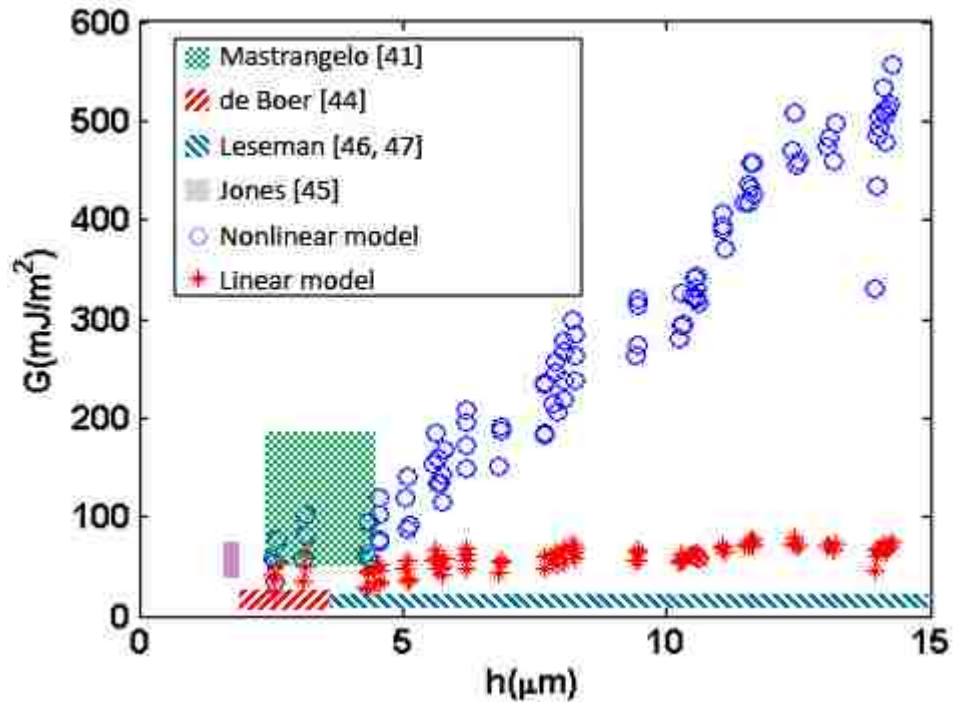


Figure 28: Example of the type of fit attained using the nonlinear model

The method developed in Section 2.2 is applied to the data gathered and is plotted in Figure 29. This figure displays data for 7  $\mu$ cantilevers only, though more data was collected. Displaying of additional data would make plots unnecessarily difficult to read and not add additional information. This data is analyzed two different ways. The asterisks represent the strain energy release rates calculated using linear modeling assumptions (10) but using the  $M_0$  from (4) - (8). The circles represent values obtained by using the nonlinear method developed here.



**Figure 29: *The strain energy release rate increases as the crack propagates with increase in height***

The discussion of the previous results are broken into two sections. First a theoretical section discusses the results of the new nonlinear formulations and its applicability to determination of  $G$  values in comparison to the previously used linear

formulations. The second subsection discusses the experimental findings. Specifically, the model is applied to data and conclusions are drawn about how well the model works to match experimentally measured deflections and report  $G$  values. Additionally, a discussion ensues about how  $G$  can vary as a function of surface conditions and loading. Results from this work include values for  $h$  larger than previously reported and it is concluded that the loading condition of the structure dramatically affects the value of  $G$  due to surface roughness.

### 5.1.1 Modeling Discussion

The main results of the modeling are the nonlinear beam theory Section 2.1 and determination of the strain energy release rate. Figure 3 compares the solutions for a fix-fix beam whose ends are at different heights,  $h$ , for the linear case (deflections/rotations small and no centerline stretching) and the nonlinear case (deflection/rotations small and centerline stretching). This particular plot is for a beam whose thickness is  $2.3 \mu\text{m}$ . After a value of  $323.6 \text{ nN}$  it can be seen that  $F_y$  for the nonlinear model varies by more than 5% after an  $h > 622 \text{ nm}$ . This result can be generalized to reflect that any beam with fix-fix end conditions can have its deflection modeled using a linear model if  $h \leq 0.2707t$ . For larger values of  $h$ , the nonlinear model must be used to avoid large errors in modeling the deflection profile of the beam. Of course the nonlinear model is applicable for  $h \leq 0.2707t$  as well. Figure 28 shows a  $\mu$ cantilever beam with fix-fix ends that has  $h = 3.96 \mu\text{m}$ . The RMS Error for the nonlinear model's fit to the experimental data is  $1.23 \text{ nm}$ . For the case of the linear model its RMS error is  $23.31 \text{ nm}$ . The nonlinear beam model is more accurate than the linear model for the entire range of  $h$ . As  $h$  is increased, the RMS error for both the nonlinear model and linear model increase linearly. However the linear

model's RMS error increases 2.2 faster than the nonlinear model. Clearly, considering axial stretching ( $F_x$  development) of the beam leads to more accurate solutions for the deflection profile of the  $\mu$ cantilevers.

The nonlinear beam model yields values for  $F_x$ ,  $F_y$ , and  $M_\theta$ . Immediately, one realizes that development of  $F_x$  implies that for relatively large  $h$  values stiction failure must be considered to be a Mixed Mode (I & II) fracture problem. Previously it was considered to only be a Mode I problem.  $F_x$  can be determined using (11). Figure 30 demonstrates how the the axial stress,  $\sigma_x$ , develops in the cantilever beam array (CBA) method as  $h$  increases. Due to these relatively large longitudinal stresses, a considerable shear component is imparted at the  $\mu$ cantilever substrate interface, which will lead to Mode II type fracture. Note that the formulation for the strain energy release rate developed in Section 2.2 are robust and capture the strain energy in the deformed beam that contributes to both Mode I and II types of fracture.

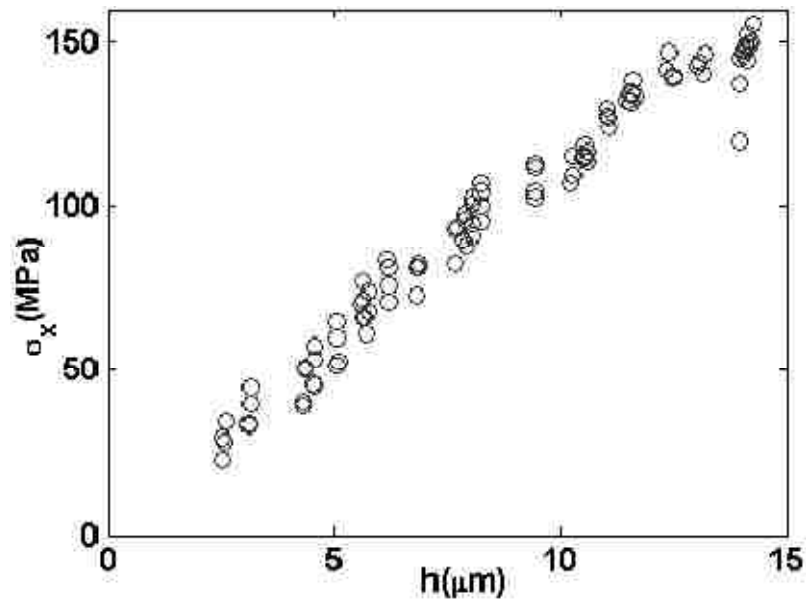


**Figure 30:** Longitudinal stress that develops in the  $\mu$ cantilevers as a function of height



In order to determine  $G$ , the elastic strain energy stored in the beam must be determined. Prior to this work, researchers assumed that all elastic strain energy stored in the beam was due to bending (see (10)). However, the nonlinear model shows that contributions due the forces,  $F_x$  and  $F_y$ , are considerable and dominate for relatively large values of  $h$ . Energy methods were used, in order to fully account for the strain energy stored due to all three contributions from  $F_x$ ,  $F_y$ , and  $M_0$ . These methods were found to be consistent and, as expected, show that more strain energy is stored in the  $\mu$ cantilevers than was previously thought due to inclusion of all contributions to  $U$ .

In order to better understand the difference between the new model for  $G$  that incorporates the nonlinear beam model and energy method, it is compared to the prior method that utilized the linear beam model which is used in conjunction with (10). For the linear case of  $G$  one finds that  $G \propto \frac{h^2}{s^4}$ , (see (1)) while for the nonlinear case  $G \propto \frac{h^6}{s^4}$ , this was attained by using the Taylor's series expansion of (4) - (6) in order to find  $G$ . Note that both the linear and nonlinear models are dependent on  $s$  in the same manner, but the nonlinear model is  $h^4$  more dependent on  $h$ . This is a direct result of considering longitudinal extension of the beam. Thus  $G$  values predicted by the nonlinear model are expected to be higher than those previously reported due to an increased sensitivity of  $G$  to  $h$ . In summary, the values for  $G$  reported previously are expected to be low because they did not consider the nonlinear deformation of the beam and all contributions to the strain energy.

### 5.1.2 Experimental Discussion

The results of the experiments after analysis with the new theory yields two main results. First, values found with the new procedure are on average higher than those previously reported. Secondly,  $G$  increases with increasing height of the base,  $h$ , above the substrate. The following discussion details insight on each of these topics.

The average value for the newly derived model is higher than previous reports. Figure 29 shows one set of data analyzed two different ways. The asterisks represent the values attained using (1) with  $M_0$  calculated using (4) - (6). Thus the  $G$  found here uses the more accurate formulation for the deflection of the beams, (4), but with the assumption that the strain energy is due only to bending. With this more accurate determination of the moment,  $M_0$ , it is found that  $G$  is larger than previous reports. This is attributed to more accurately capturing  $s$ , due to the 700+ data points per beam, and more accurately determining  $M_0$  with the nonlinear beam deflection model.

The circles of Figure 29 are found using the full model previously described, including the effects of  $M_0$ ,  $F_x$ ,  $F_y$  in calculating the strain energy as developed in Section 2.2. The blue circles have a similar value for  $G$  as do the asterisks for small values of  $h$ . As  $h$  is increased the value for the nonlinear formulation (circles) increase somewhat linearly. This effect is due to the consideration of the normal forces and shear forces on the substrate. This increase for the value of  $G$  as a function of  $h$  is somewhat surprising, but can be understood after some thought is given to the surface and loading conditions.

The bottom side of the beam has an average roughness of 24.94 nm and the substrate has an average roughness of 4.27 nm. This has been independently verified by the authors using an AFM and also corroborated by other reports [60]. Because there is

surface roughness, the entire area of the  $\mu$ cantilever beam does not come into intimate contact with the surface below it. Thus contact occurs at asperities which has been the study of numerous other researchers [50], [61], [62], [63]. The important consideration for the current work is the existence of the asperities. The amount of contact between the two surfaces is therefore due to the forces applied between the  $\mu$ cantilever and the surface. For small values of  $h$  this value is relatively low. As  $h$  increases the value of  $F_y$  and  $M_\theta$  both increase monotonically. Thus the two surfaces are pressed together more intimately. More specifically, if the asperity contacts can be considered to be Hertzian in nature then as  $F_y$  increases linearly the area of contact increases proportionally between the surfaces as  $A^{3/2}$ .

The final consideration is static friction (stiction) at the interfaces of the asperities. During separation of the cantilever from the substrate the horizontal asperity faces resist the separation due to the chemical bonds present between the molecules. The vertical asperity faces, on the other hand, are in shear. In this case the axial force that develops,  $F_x$ , is the primary factor. The shapes and size of the bumps are random but in order to simplify the statistical nature of their distribution one may try to imagine a surface like Figure 31. In this figure  $F_x$  represents the longitudinal force in the cantilever,  $N$  is the normal force developed between the walls of bumps and  $F_f$  represents the friction force. This is a simplified model but sufficient enough to give insight on the role of friction during crack development. The following shows that friction can be responsible for a noticeable portion of the difference between the  $G$  reported here (Mixed Mode) and the values reported for small  $h$ 's (mainly Mode I).

The longitudinal force of the  $\mu$ cantilever is responsible for the normal force on the surfaces. The friction force does a specific amount of work during the slippage. Following the same procedure used to find the strain energy release rate one can specify the portion of  $G$  that is actually not due to elastic energy stored in the beam but due to friction.

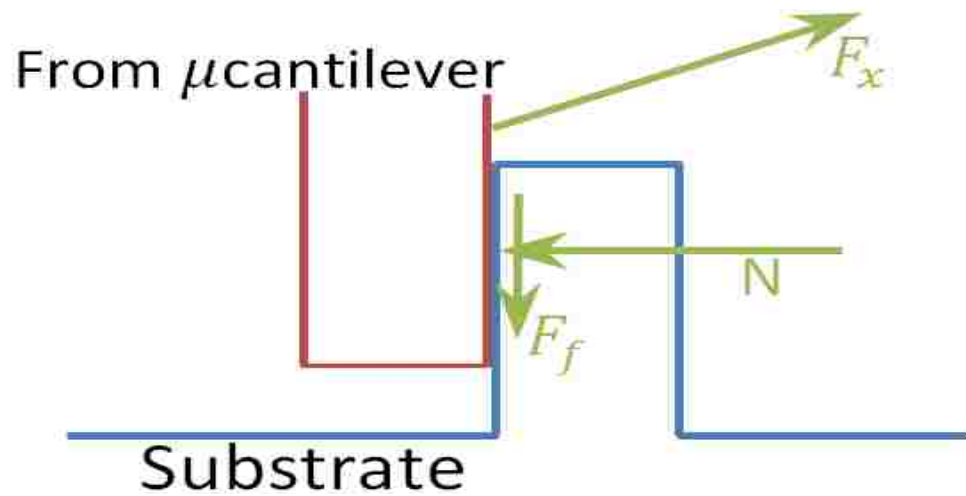


**Figure 31:** *The simplest model to study the role of friction is to consider the surfaces to be interlocked as shown. In general not all portions of the contacting surfaces can be modeled to be composed of normal and vertical surfaces but the proposed analysis can be used to attain sufficient insight on the role of friction*

$$G_f = \frac{1}{w} \frac{\partial W_f}{\partial s} \quad (26)$$

where  $W_f$  is the work of friction which is equal to  $W_f = \mu N \delta y_{(x=0)}$ . Substituting in (26):

$$G_f = \frac{1}{w} \frac{\partial W_f}{\partial y_{(0)}} \frac{\partial y_{(0)}}{\partial s} \quad (27)$$

$$G_f = \frac{1}{w} \mu N \frac{\partial y_{(0)}}{\partial s} \quad (28)$$

$$G_f = \frac{1}{w} \mu F_x \cos\left(y'_{(0)}\right) \frac{\partial y_{(0)}}{\partial s} \quad (29)$$

Figures 32 and 33 show the friction force,  $F_f$ , and  $G_f$  calculated using the average bulk silicon friction coefficient ( $\mu = 0.3$ ) [64]. Comparing Figure 32 by Figure 29 it is seen that  $G_f$  is responsible for a noticeable portion of  $G$ . This portion is not due to stored energy in the beam but due to dissipative work of stiction. The main reason for  $G_f$  is the longitudinal force developed in the  $\mu$ cantilever during the peel test and is not expected to be observed in macro-scale crack propagation since ideally the sample is free to move in plane and no longitudinal forces are present in macro scale tests. Although the work done by stiction is dissipative in nature, the friction developed by longitudinal forces of the cantilever also has the effect of increasing the contact quality on the adjacent faces. So even after subtracting the frictional contribution from the total strain energy release rate, one should not expect to have the role of inherent Mode II disappear and to get a constant  $G$  value. This is shown in Figure 34.

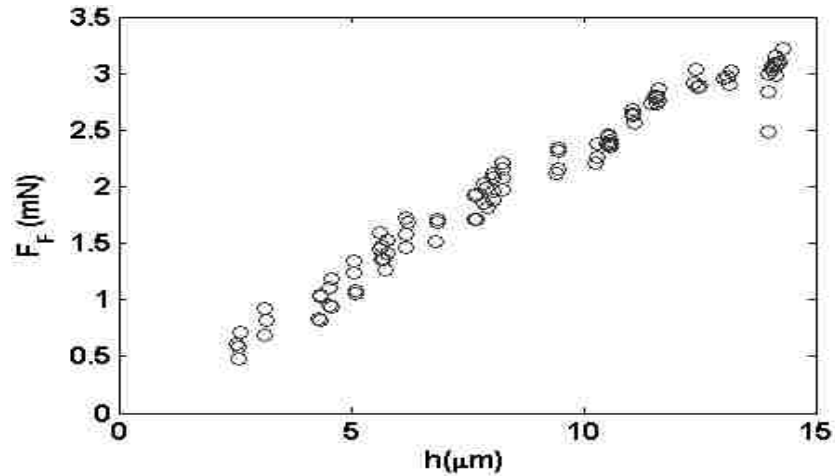


**Figure 32:** *The friction force on the side faces of the bumps as the slide on top of each other during the crack propagation. The friction force represented here is obtained considering the macroscopic friction coefficient to hold at the microscale*

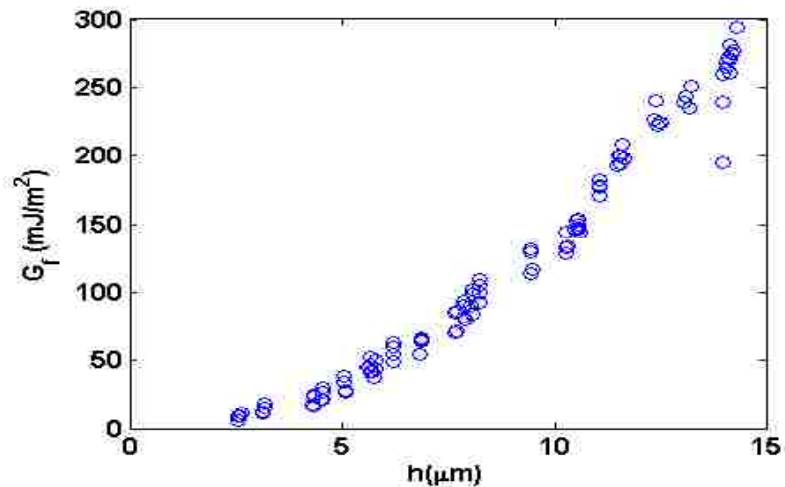


**Figure 33:** *The values of  $G_f$  presented here shows the portion of the strain energy release rate that is due to the friction on sliding faces of the bumps. This portion is not due to the elastic strain energy stored in the beam and should be subtracted from the total strain energy calculated.  $G_f$  is not present in macro-scale mode I crack propagation. The reason that it is seen in the macrocantilever test is due to large longitudinal force developed in the cantilever*

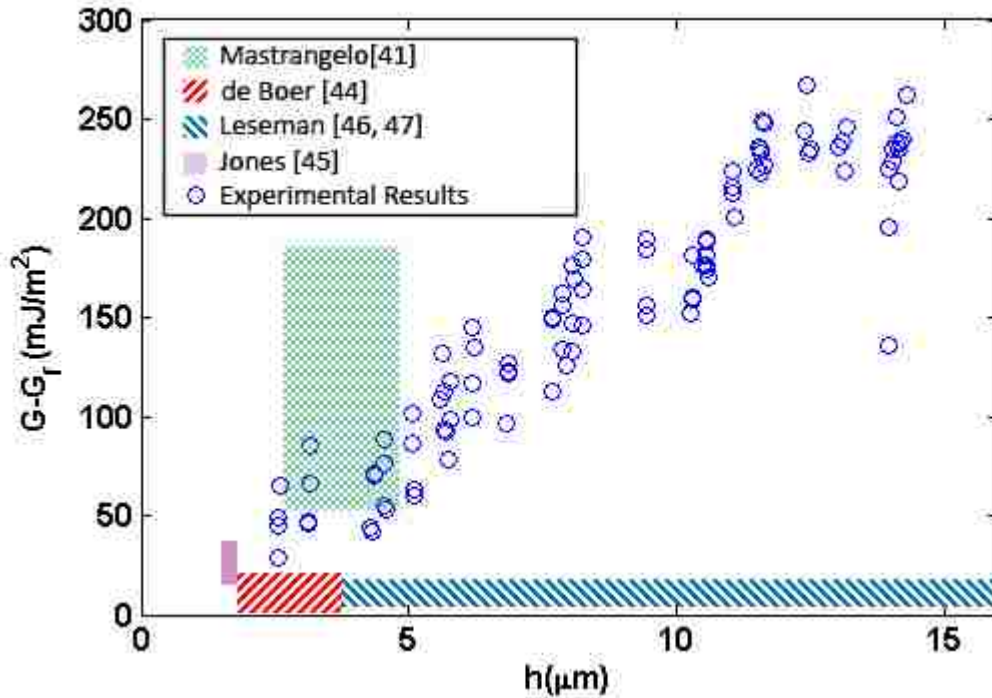


**Figure 34:** *Although it was shown that friction is responsible for a considerable portion of  $G$  but even after subtracting  $G_f$  from the total strain energy release rate one should not expect to get a constant value for strain energy release rate. The reason is due to the effects of loading*

### 5.1.3 Practical Considerations

For these sets of experiments poly-Si microcantilevers and substrates were used from the SUMMiT V process. Much of the data from previous reports comes from using the SUMMiT process [10], [38], [44], [46], [47], [50], [56], [45]. SUMMiT V is one of the most common methods to produce surface micromachined MEMS devices. Using this process the height difference between a poly-Si layer and the substrate can be as high as 10.75  $\mu\text{m}$  or as small as 300 nm, see Figure 11. In this work, the strain energy release rate is studied up to a height of  $h = 14.2 \mu\text{m}$ . It is shown that the beams behave linearly only

up to  $h = 622$  nm. This range of measurements covers the entire range of fabrication heights for devices in the SUMMiT process and most other processes currently used.

An additional consideration is use of this model for devices that fail during service. Typically,  $h$  is at a fixed height and does not vary as in the peel test. Usually a  $\mu$ cantilever will fail initially in an arc-shaped failure mode [44] and upon additionally application of force will fail in an  $s$ -shaped manner. This transition from an arc to an  $s$ -shaped failure mode will cause the  $\mu$ cantilever to begin to store tensile strain energy in the failed length of the beam and the deflected length of the beam if there is no slip. The model developed in this work is robust enough to capture all of the residual strains in the deflected length of the beam because it utilizes a fit to the experimental data in order to determine the best fit for  $F_y$ ,  $M_0$ , and  $F_x$ . Using this information one could determine, based on the value of  $F_x$ , what the residual tensile strain had to be in the failed length of the beam in order to impart such a stress into the deflected portion of the beam.

The final practical comment that comes from this work is the applicability of the overall idea. Roughly speaking, for any deflection of a structure that contains more than one fixed point stretching should be considered. Devices more complex than a  $\mu$ cantilever could be modeled with finite elements and the stretching determined. Similar energy method, as those in Section 2.2, could be used in order to determine values for  $G$  in a given process.



## 5.2 Experimental Results for Mode II

### 5.2.1 Experimental Results for Upper Bounds of $G_{II}$

From the experiments the spring displacement from the vernier scale of the actuator is noted at which the cantilever beam failed on substrate is released along with the piezo readings. Curve fitting is performed on Figure 5 and force equation obtained is  $F = 72.17x + 2.674x^3$  with  $R^2$  value of 1. Thus by knowing the stiffness and the spring displacement, maximum force applied to a microcantilever before the cantilever slipped is calculated. Note that the  $155 \mu\text{m}$  length of the microcantilever that was stiction failed on the substrate starts slipping after causing the spring displacement to some position. Piezo displacement versus spring displacement curve is shown in Figure 35.

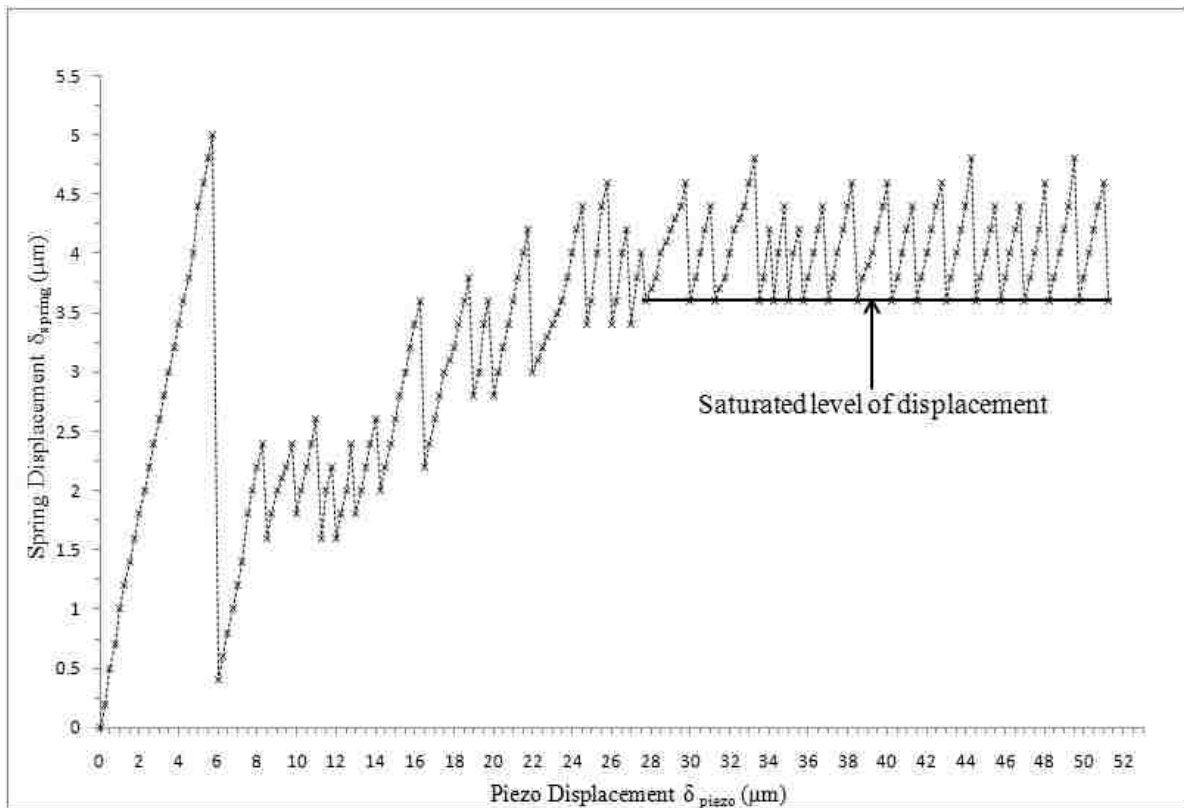


**Figure 35: Piezo displacement versus spring displacement curve**

From the Figure 35 it is observed that initially the MEMS actuator's displacement tracks the displacement of the piezo indicating that no slip is occurring. After displacing the MEMS actuator 5  $\mu\text{m}$  the microcantilever incurs a sliding failure and the MEMS actuator's displacement correspondingly decreases, but not to zero. Further increments of the piezo cause the MEMS actuator to track the piezo displacements again until another sliding failure occurs. This trend is continued throughout the experiment. It is observed that after the occurrence of a number of sliding failures (~13) the intermediate position where the microcantilever beam placed on the substrate stopped is saturated and never falls below this saturation displacement of the spring.

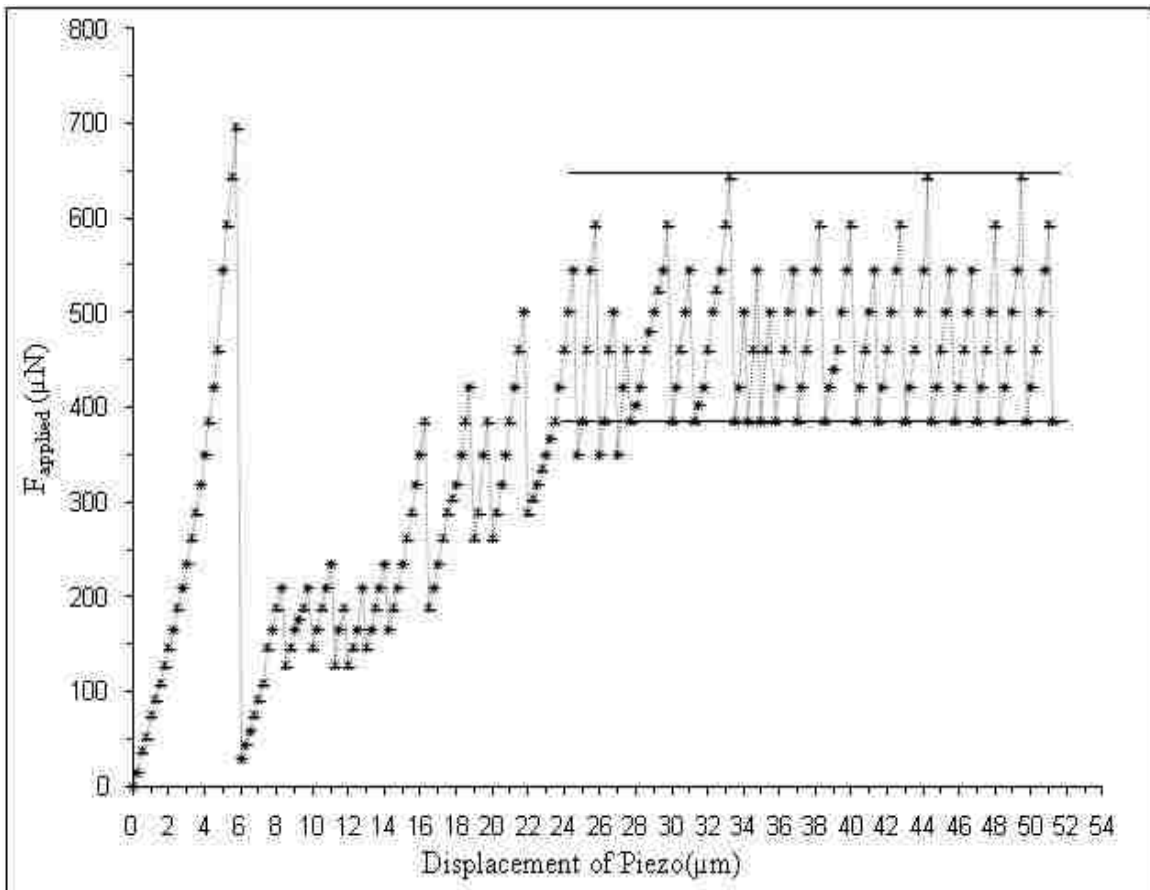


**Figure 36: Piezo displacement versus force applied curve**

From Amonton's law which states that the friction force is directly proportional to the (normal) applied load, with a constant of proportionality, the friction coefficient, that is constant and independent of the contact area, the surface roughness, and the sliding velocity. The force required to initiate sliding is known as static friction force. The static friction force can be written as  $f_s = \mu_s N$ , where  $\mu_s$  is the coefficient of static friction and  $N$  is the normal force acting due to bonding of the two surfaces. By using a coefficient of friction value of 0.35 [57], a normal force acting due to bonding is found to be approximately 2 mN. And the kinetic friction force can be written as  $f_k = \mu_k N$ , where  $\mu_k$  is a coefficient of kinetic friction and  $N$  is again the normal force acting due to the bonding of the two surfaces. Normal force acting due to bonding was found to be approximately 1 mN for kinetic friction force. The lateral force applied is equal to the static friction force when the cantilever beam starts sliding on the substrate.

Referring to Figure 36, the maximum force applied to a microcantilever before the cantilever slipped is calculated by knowing the stiffness and spring displacements. The initial maximum force recorded before the microcantilever beam slipped is the static friction force. It is observed that initially the static friction force required to initiate sliding is larger than the kinetic friction force required to sustain sliding. The static friction force is high due to larger contact area. As we have seen from the Figure 35, after the occurrence of slip between microcantilever beam and substrate, it did not return to its zero position and stopped at an intermediate position. We believe that secondary bonds are formed once the cantilever beam starts sliding which lead to kinetic frictional force. Values for the kinetic frictional force varied initially until the intermediate position is saturated, but once the saturation level is reached then the kinetic frictional force varied

almost constantly (region between the two horizontal lines shown in Figure 36). The kinetic frictional force also reaches the static frictional force even though the contact area is smaller compared to the initial position.

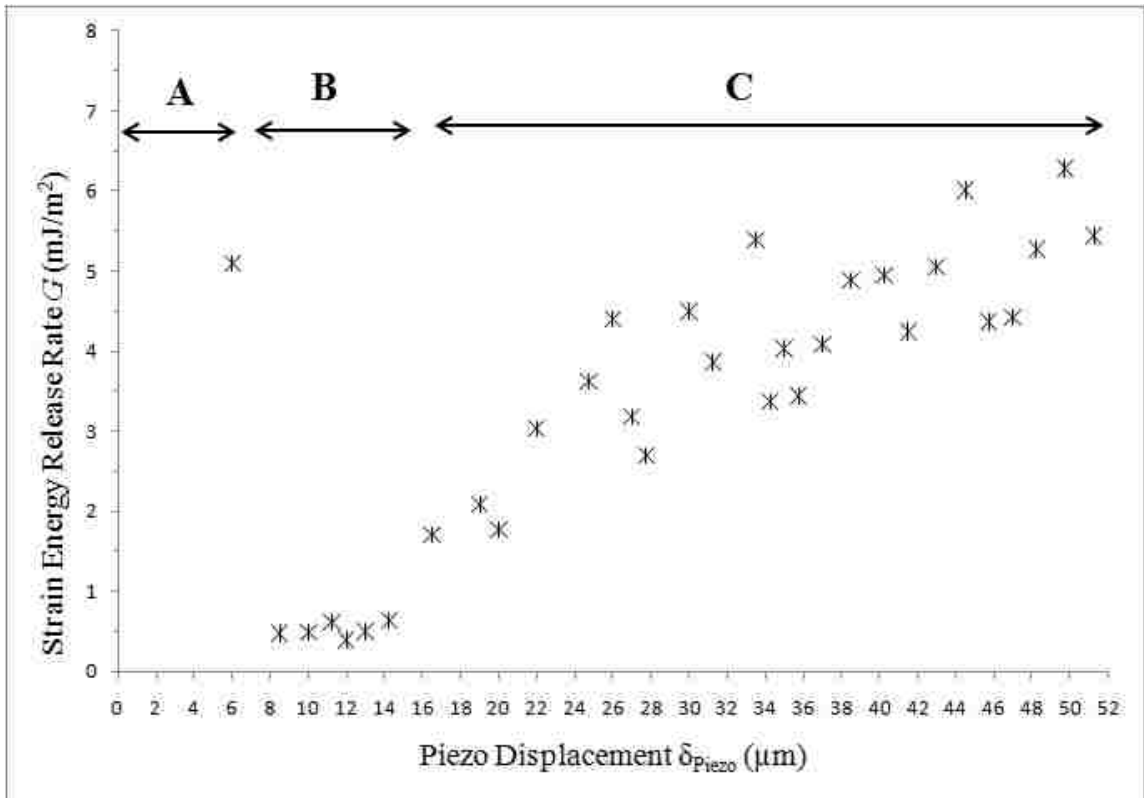


**Figure 37: Piezo displacement versus  $G$  curve**

The maximum force applied to the cantilever is used in (18) of Section 2.3.1 to calculate the upper bounds strain energy release rates from Mode II type failures. Note that the 155  $\mu m$  length of the microcantilever beam placed on the substrate releases upon application of this force and stops at an intermediate position. Again the maximum force applied to the cantilever placed at an intermediate position is used to calculate strain energy release rate. This trend is continued and each time the maximum force applied to the cantilever beam placed on the substrate to release is used to calculate strain energy

release rates and thus the critical strain energy release rates calculated here is for the value of initiation of a crack in Mode II. Additionally, because the crack grows through the entire length of the beam, it is uncertain where the crack will arrest. Clearly, it would continue to grow had there been a longer beam. Thus the following results are the upper bounds for the critical strain energy release rates of Mode II failure.

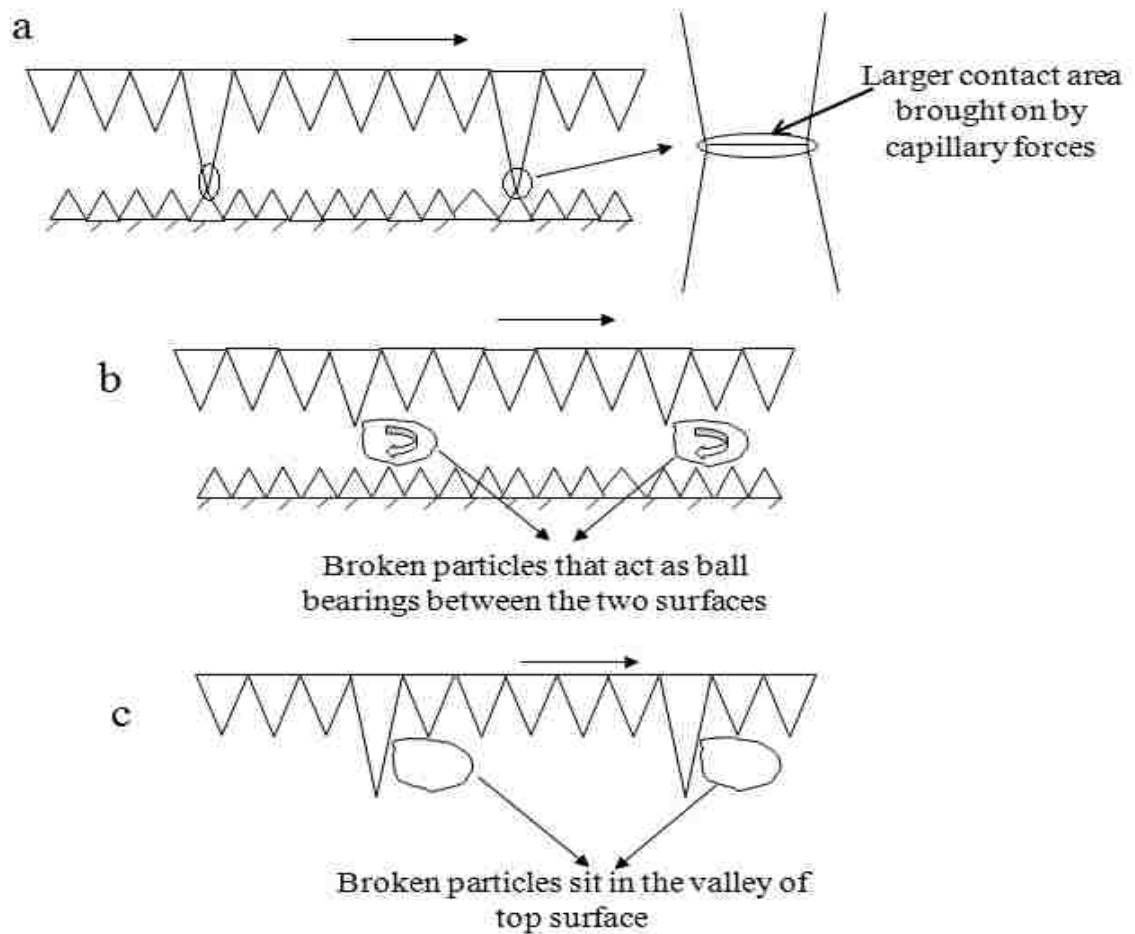


**Figure 38:** *An example of two rough surfaces in contact, (a) Larger contact area brought on by capillary forces (b) An image where broken particles acting as ball bearings between the two rough surfaces (c) An image where the broken particles sit in the valley of top rough surface*

Referring to Figure 37, the high strain energy release rate found in region A is due to the larger contact area brought on by capillary forces (see Figure 38a) and also due to the mechanical interlocking between the peaks of two rough surfaces that are brought in contact with each other. The strain energy release rate has dropped in region B, as the peaks that broke off are moving in the gaps of two rough surfaces (see Figure 38b) which are acting like ball bearings and by rolling between the two rough surfaces, which causes easier sliding of the microcantilever beam on the substrate, thus resulting in low strain energy release rates in region B. It is observed that the strain energy release rates are again increased in region C, as the peaks that broke off sit in the valley of the top surface (see Figure 38c), this is confirmed after making the surface roughness measurements of substrate side (bottom) of the microcantilever is made on the area where the microcantilever beam made contact with the substrate onto which it was failed and the bottom of the microcantilever beam where no contact was made is measured. The increase in a RMS roughness value of substrate side (bottom) of the microcantilever on the area where the microcantilever made contact with the substrate onto which it was failed confirmed the presence of larger particles in the valley of the top surface. A complete discussion of the surface roughness is given in Chapter 6. The strain energy release rates become constant as the particles get saturated at a place.

Using  $E = 150 \text{ GPa}$ , we find that the average value of interfacial adhesion energy is  $G_{II} \leq 4.387 \frac{\text{mJ}}{\text{m}^2}$ . This value agrees with our earlier experiments Section 5.1 that included mixed mode (Mode I and II) effects. It should be mentioned that these experiments were carried out in a cleanroom, at a humidity levels of below 46% and at a temperature of  $70.6^\circ\text{F}$ .

### 5.2.2 Experimental Results for an Exact Value of $G_{II}$

From the experiments the spring displacement from the vernier scale of the actuator is noted as  $5.2 \mu\text{m}$  at which the  $\mu\text{cantilever}$  beam failed on substrate is released and onset of crack growth is observed. Figure 39 shows the various curves that are drawn using experimental data points taken from the interferometric data. An increment in crack is observed with every increment of piezo in  $-x$  direction as explained in Section 4.3.1. The length and height of the  $\mu\text{cantilever}$  beam raised at the fixed end are plotted in Figure 39. Figure 40 shows the region of interest of Figure 39, where we can see the crack growth for every increment with piezo displacement.

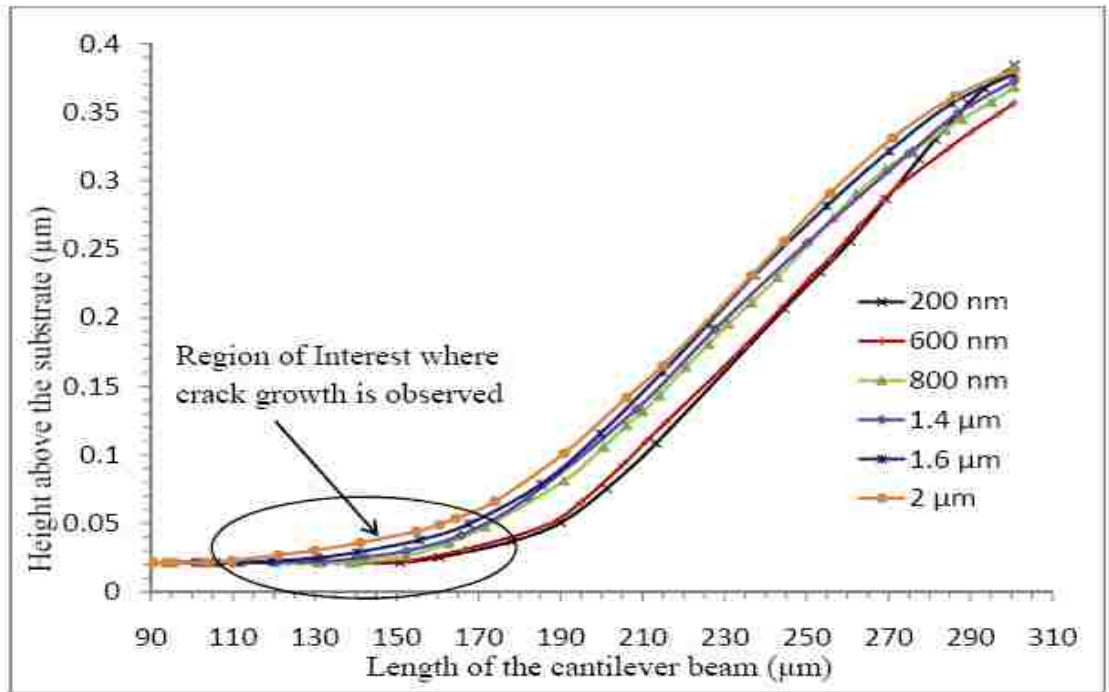


**Figure 39:** Length of the  $\mu\text{cantilever}$  beam versus height raised at fixed end of the beam

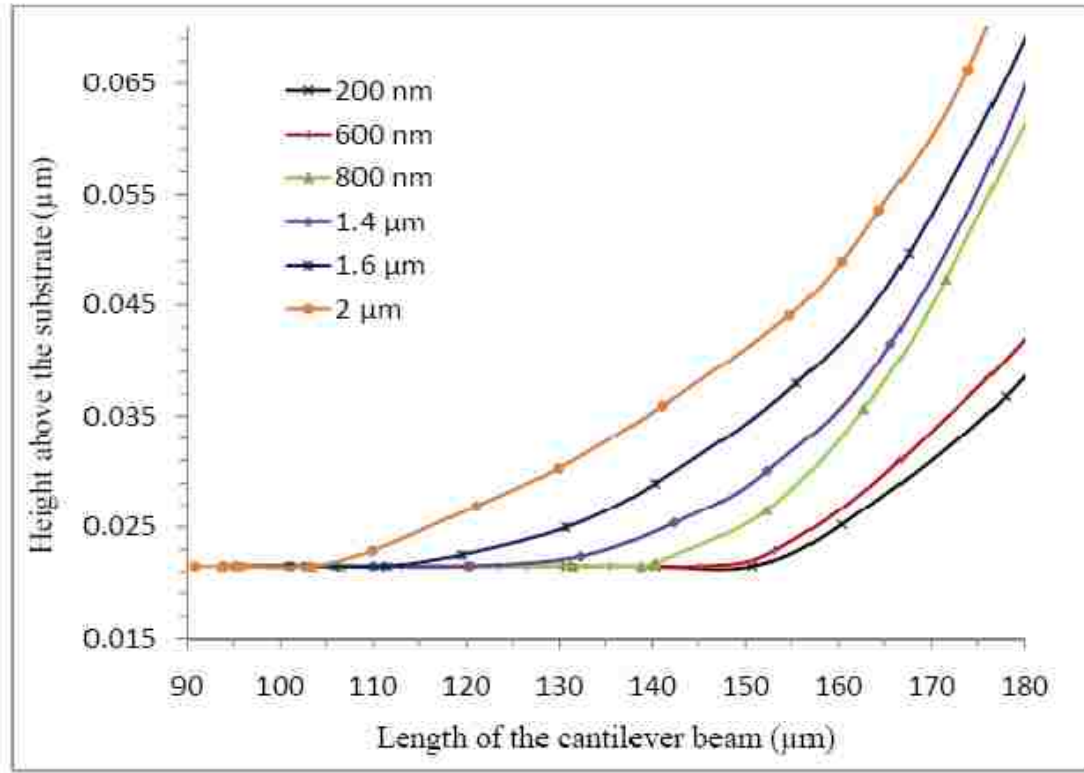


**Figure 40: ROI of figure 39 which shows the crack growth with every increment of piezo**

Using the force equation obtained earlier by curve fitting i.e.,  $F = 72.17x + 2.674x^3$  with  $R^2$  value of 1. Maximum force applied to a microcantilever before the spring is released is calculated as 751  $\mu\text{N}$ . The maximum force applied to the cantilever is used in (25) of Section 2.3.2 to calculate strain energy release rate from Mode II type failures. Note that the infinitesimal crack growth is seen with every 200 nm increments of piezo displacement in  $-x$  direction and thus the interfacial adhesion energy calculated here is an exact value for the  $G_{II}$ . The following result is the exact interfacial adhesion energy of the Mode II fracture problem. Using  $E = 150 \text{ GPa}$ ,  $w = 29.63 \text{ }\mu\text{m}$  and  $t = 2.3 \text{ }\mu\text{m}$ , we determined that the value is  $G_{II} = 0.932 \frac{\text{mJ}}{\text{m}^2}$



For the infinitesimal crack growth experiments, the height at the base of the microcantilever is raised by 525 nm as explained in experimental procedure Section 4.3.2. By raising the fixed end (microcantilever beam end which is welded to MEMS actuator), the shape of the beam will be an *s*-shaped beam as shown in Figure 26. In an effort to know the importance of elastic energy stored in the microcantilever due to bending and also due to tensile load acting on it, elastic energies stored are measured. Elastic stored in the microcantilever beam due to bending is calculated as  $U_{\text{bend}} = 7.66 \times 10^{-15}$  J and the elastic energy stored in the microcantilever due to tensile load acting on it is calculated as  $U_{\text{tensile}} = 2.73 \times 10^{-11}$  J. It is found that the elastic energy stored in the microcantilever beam only due to bending is four orders less than the elastic energy stored in the microcantilever beam due to tensile load acting on it. As the elastic energy stored in the microcantilever beam due to bending is only 0.028% of the elastic energy stored in the microcantilever beam due to tensile load acting on it, the effect of bending in calculation of an exact value for the strain energy release rate  $G_{II}$  is negligible.

Table 1: Critical strain energy release rate  $G_C$  for a wide range of various materials

[65]

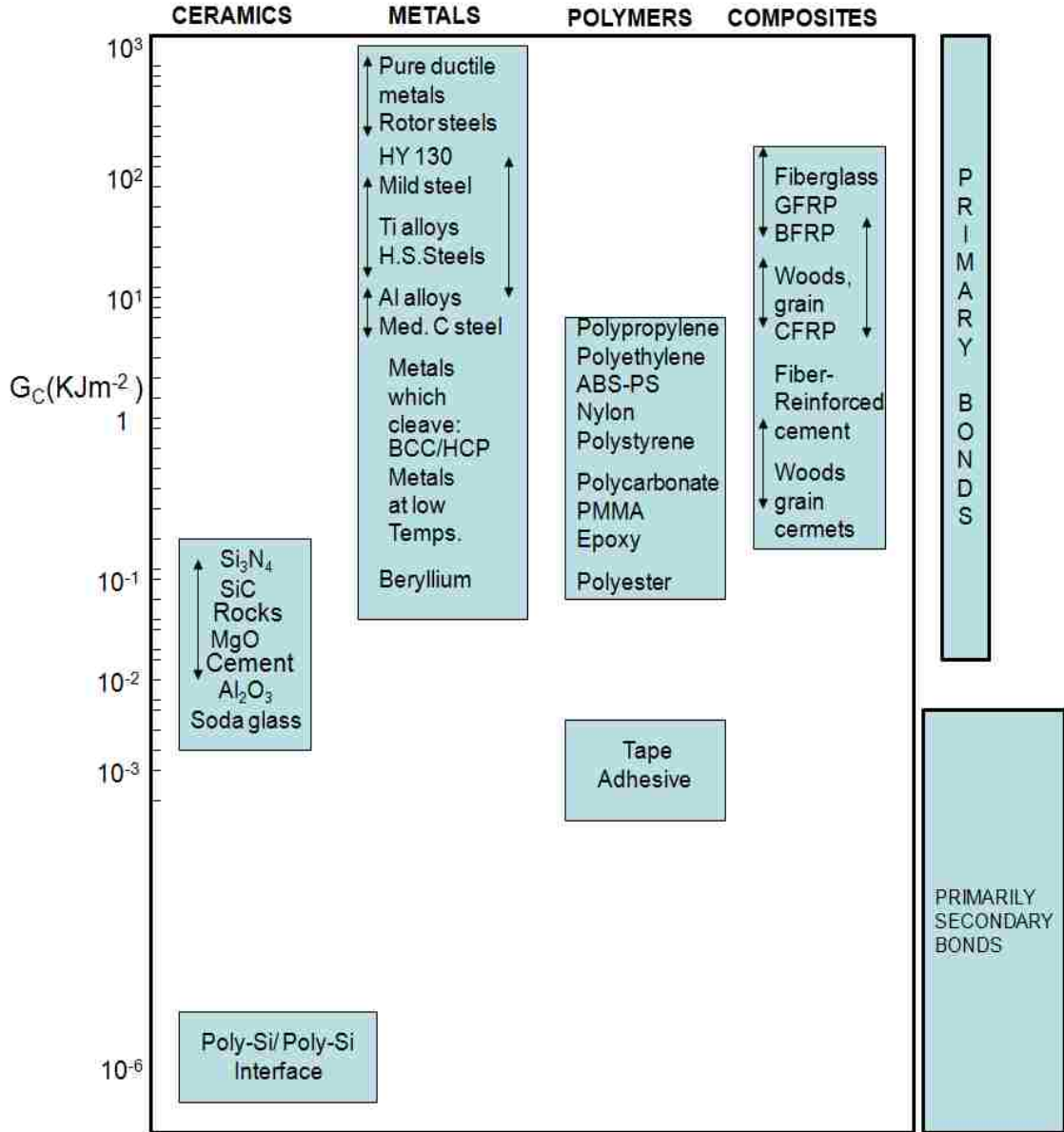


**Table 2: Comparison of Strain Energy Release Rates  $G$**

<b>Author</b>	<b>Title, Publication, Year</b>	<b>Type of study, Treatment, Conditions etc.</b>	<b>Strain Energy Release Rates <math>G</math> (mJ/m<sup>2</sup>)</b>
Mastrangelo <i>et al.</i> ,	A simple experimental technique for the measurement of the work of adhesion of microstructures, <i>IEEE</i> , 1992.	CBA method and detachment lengths of shortest beam in an array. HF treated microcantilever beams. Hydrophilic samples	140
Mastrangelo <i>et al.</i> ,	Mechanical stability and adhesion of microstructures under capillary forces - Part II: Experiments," <i>JMEMS</i> , 1993.	CBA method, prediction of detachment lengths from the plot of detachment length as a function of beam parameters. HF treated microcantilever beams. Hydrophilic samples	270
de Boer <i>et al.</i> ,	Accurate method for determining adhesion of cantilever beams, <i>Journal of Applied Physics</i> , 1999.	CBA method, Fracture mechanics model under displacement control conditions. HF treated microcantilever beams. Hydrophilic samples	16.5
Jones <i>et al.</i> ,	Adhesion of micro-cantilevers subjected to mechanical point-loading: Modeling and experiments," <i>Journal of Mech. Phys. Solids</i> , 2003.	CBA method, Mechanical point-loading. HF treated microcantilever beams. Hydrophilic samples	20.6
Leseman <i>et al.</i> ,	Experimental Measurements of the Strain Energy Release Rate for Stiction-Failed Microcantilevers Using a Single-Cantilever Beam Peel Test, <i>JMEMS</i> , 2007.	CBA method, Cantilever beam peel test. HF treated microcantilever beams. Hydrophilic samples	15.4
Hurst <i>et al.</i> ,	A New Method to Determine Adhesion of Cantilever beams Using Beam Height Experimental Data, <i>Tribol Lett.</i> , 2009.	Undisclosed	0.628
Mousavi <i>et al.</i> ,	Improved Model for the Adhesion of $\mu$ cantilevers: Theory and Experiments, <i>JMEMS</i> , unpublished.	CBA method, Peeling of cantilever beams. Nonlinear Model. HF treated microcantilever beams. Hydrophilic samples	600

## CHAPTER 6

### ROUGHNESS ANALYSIS

The surface roughness plays an important role in the adhesion of MEMS structures; hence it is very important to measure the surface roughness. Using a Veeco Nanoscope3 Atomic Force Microscope (AFM) the surface roughness of the microcantilever beams and substrates were characterized. All measurements were made in air using tapping mode. AFM cantilever tips used consisted of 1-10 Ohm-cm phosphorus (n) doped silicon. The dimensions of the cantilever tips used are 115-135  $\mu\text{m}$  long, 30-40  $\mu\text{m}$  wide and 3.5-4.5  $\mu\text{m}$  thick. The operating frequency of AFM is 223-316 kHz and drive amplitude is 30.00 mV. The spring constant ( $k = 20\text{-}80 \text{ N/m}$ ) is employed during the measurements. The front side of the AFM cantilever tip is not coated and back side is coated with  $50 \pm 10 \text{ nm}$  Al in order to increase reflectivity of the AFM tip. A constant scan rate of 2 Hz was utilized for all scans. Surface roughness of the various regions that were characterized is shown in Figure 41.

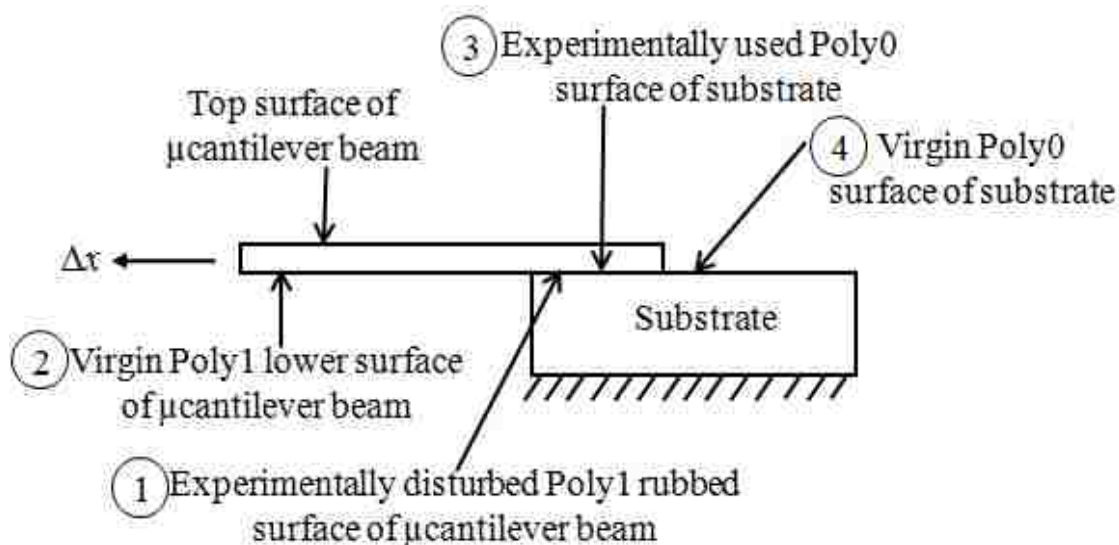


**Figure 41:** Schematic showing the various regions that are characterized

Following is the roughness data measured in sequence according to Figure 41. From Figure 41, four regions that were characterized are, first region is the experimentally disturbed Poly1 rubbed surface of  $\mu$ cantilever beam, second region is a virgin Poly1 lower surface of  $\mu$ cantilever beam, third region is an experimentally disturbed Poly0 surface of the substrate and the fourth region is a virgin Poly0 surface of the substrate.

### **6.1 Roughness Analysis of Microcantilever Beam**

In this section the surface of the microcantilever beam is measured. In particular, two measurements are made for the Regions 1 and 2 shown in Figure 41. First a measurement of the surface roughness of substrate side (bottom) of the cantilever is made on the area where the microcantilever made contact with the substrate onto which it was failed, which is an experimentally disturbed Poly1 rubbed surface of  $\mu$ cantilever beam (see Figure 41 Region 1). This data is contained in Figures 42-44. Second, the bottom of the microcantilever where no contact was made, which is virgin Poly1 lower surface of microcantilever beam is characterized (see Figure 41 region 2). This data is contained in Figures 45-47. This area is considered to have the same roughness as the microcantilever where contact had been made, but prior to contact.

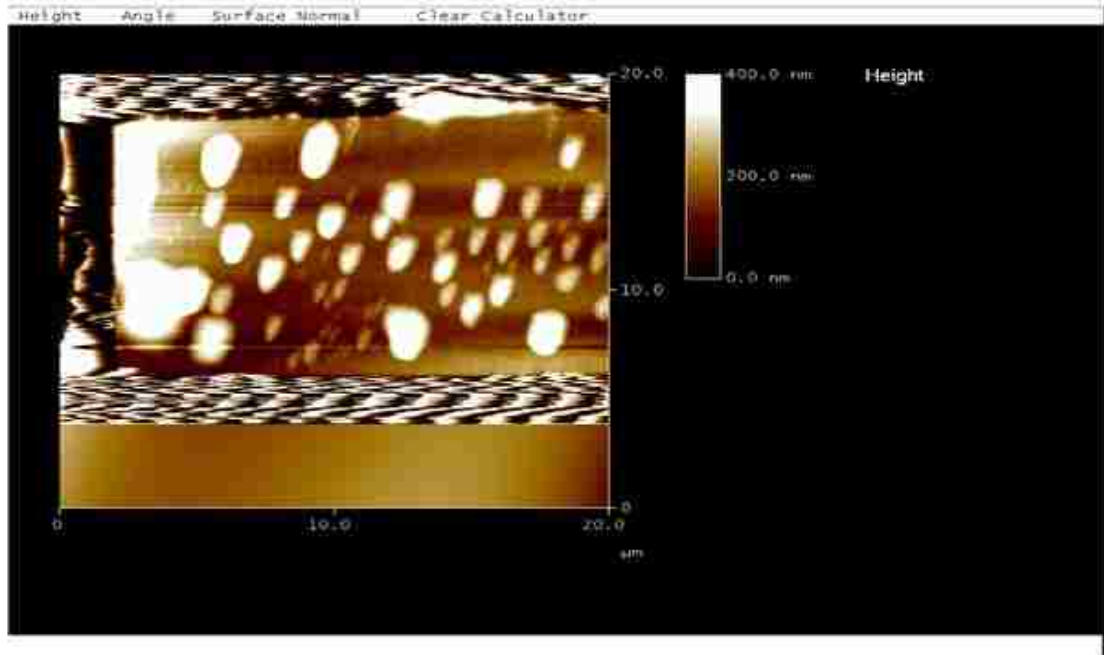


**Figure 42:** *AFM image of an experimentally disturbed Poly1 rubbed surface of  $\mu$ cantilever beam*

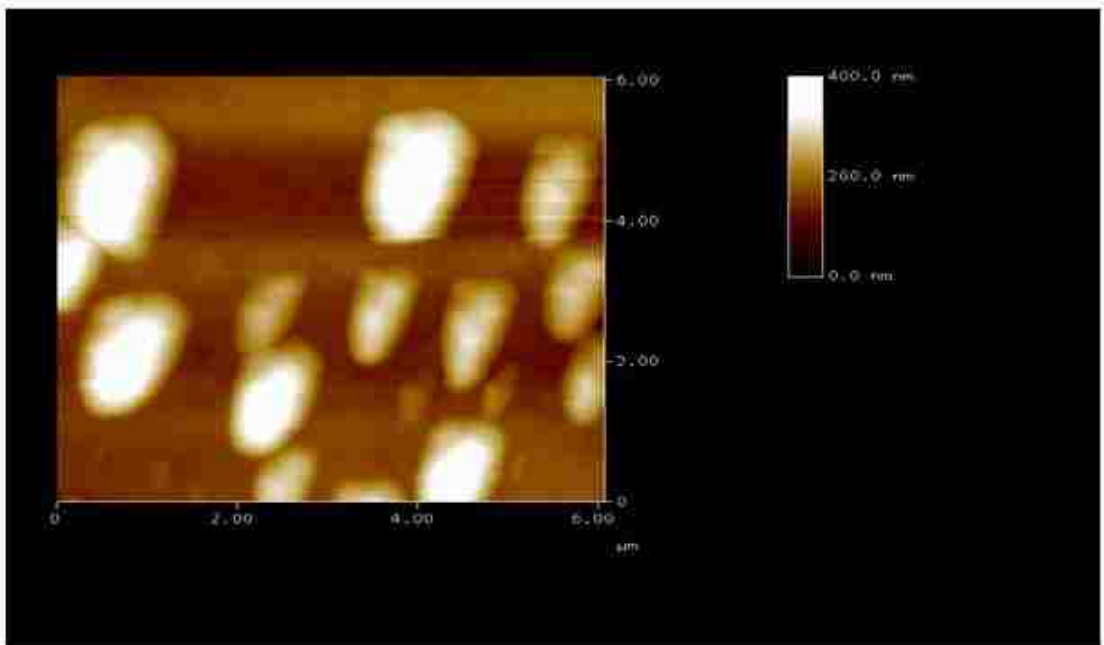


**Figure 43:** *AFM zoomed-in image of an experimentally disturbed Poly1 rubbed surface of  $\mu$ cantilever beam*

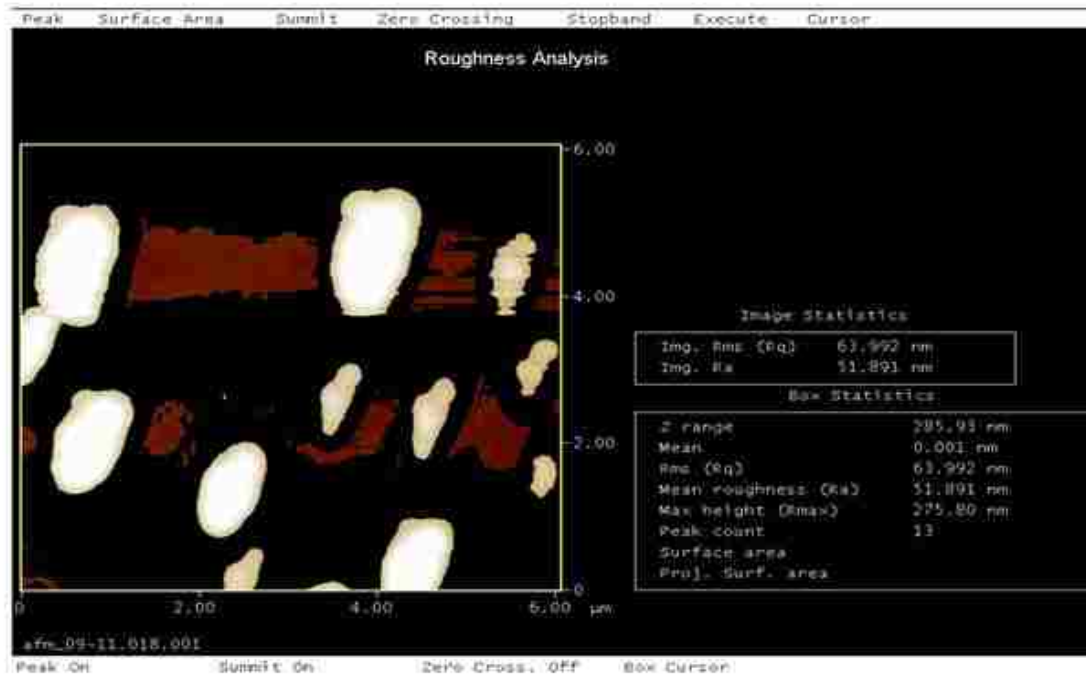


**Figure 44: AFM Roughness Analysis of an experimentally disturbed Poly1 rubbed surface of  $\mu$ cantilever beam**

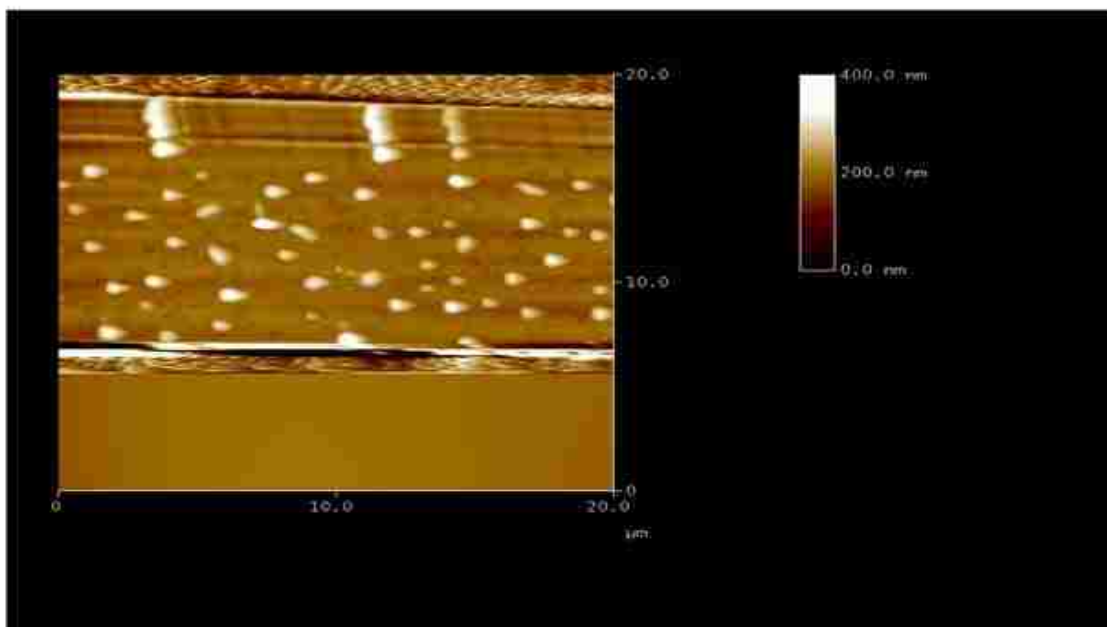


**Figure 45: AFM image of a virgin Poly1 lower surface of  $\mu$ cantilever beam**

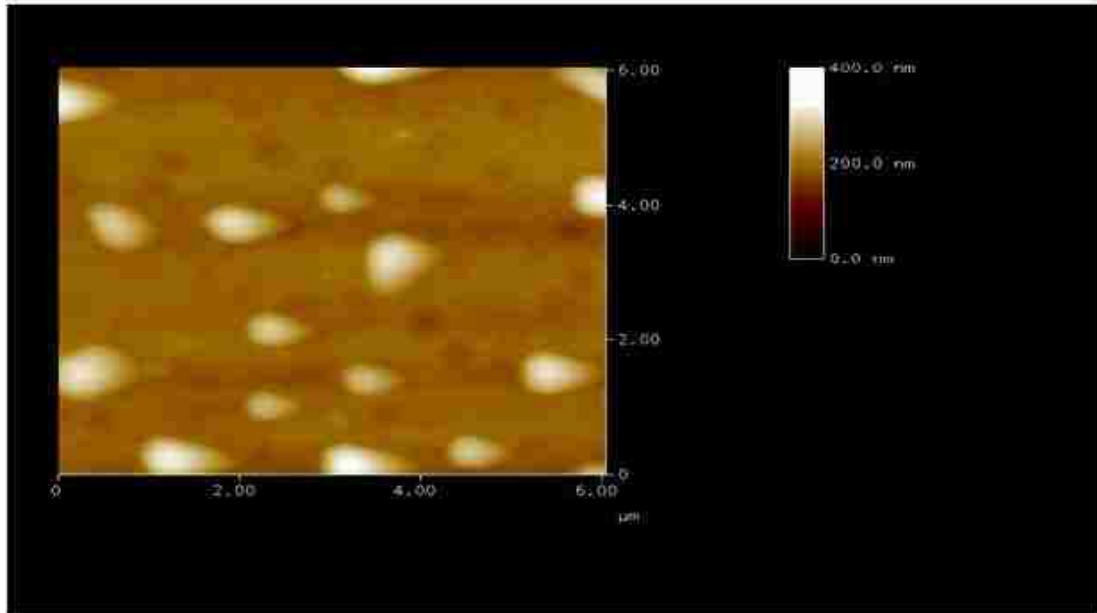


Figure 46: *AFM Image Zoomed-in image of a virgin Poly1 lower surface of  $\mu$ cantilever beam*

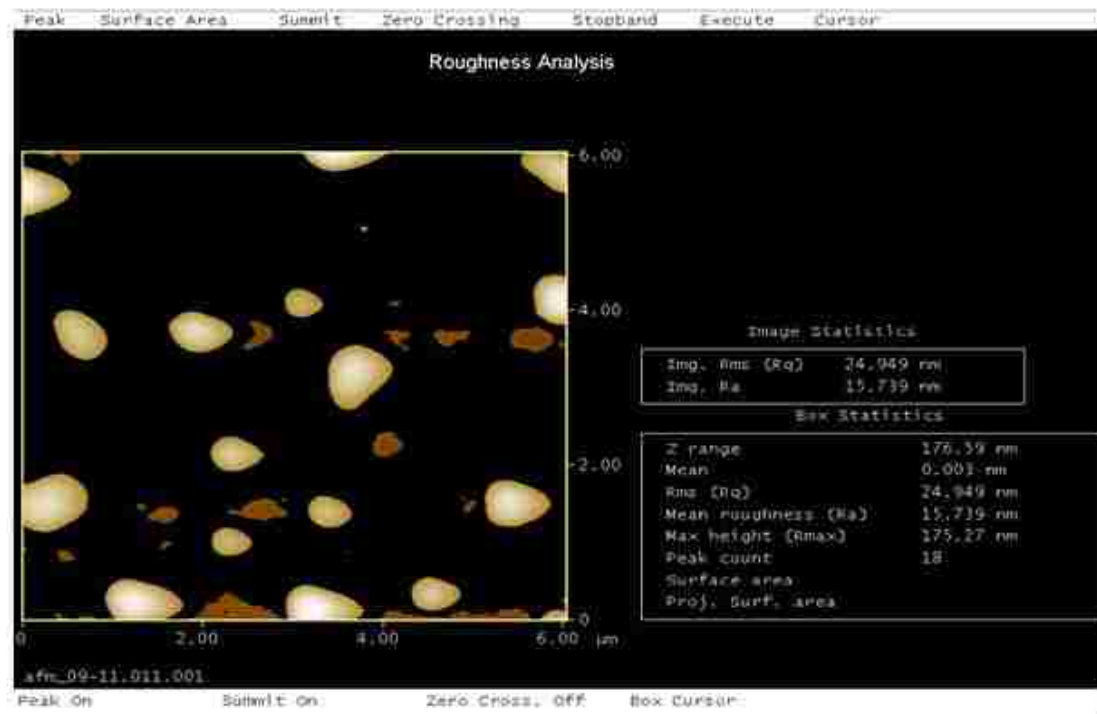


Figure 47: *AFM Roughness Analysis of a virgin Poly1 lower surface of  $\mu$ cantilever beam*



For the area that was in contact with substrate which is an experimentally disturbed Poly1 rubbed surface of  $\mu$ cantilever beam, a RMS roughness of 63.992 nm was found which has the greater roughness value compared to the RMS roughness value of the microcantilever beam (bottom side) on the area where no contact was made with the substrate which is a virgin Poly1 lower surface of  $\mu$ cantilever beam is measured as 24.949 nm. The increase in roughness is because of the peaks break off and sits in the valley of bottom surface of a microcantilever beam. The presence of larger particles is seen in Figure 44 when compared to Figure 47. Thus, a RMS roughness of the area in contact with the substrate was increased. With increase in roughness of microcantilever beam (bottom side) on the area where it made contact with the substrate onto which it was failed, and the contact area of the microcantilever beam overlapped on the substrate is decreased, the strain energy release rate is increased because peaks that broke off are resisting the motion of the microcantilever beam on the substrate. This data has been utilized in Figure 38 to explain the various regions shown in Figure 37

## **6.2 Roughness Analysis of Substrate**

In this section the surface of the substrate is measured. In particular, two measurements are made for the regions 3 and 4 shown in Figure 41. First a measurement of the surface roughness of an experimentally disturbed Poly0 surface of the substrate is made (see Figure 41 region 3). This data is contained in Figure 49. Second, virgin Poly0 surface of the substrate is characterized (see Figure 41 region 4). This data is contained in Figure 50.

To measure the surface roughness of the substrate a particular area is chosen and marked so that it is easy to locate the region where the microcantilever beam came in

contact with the substrate. In Figure 48, area inside the marked portion refers to region 3 in Figure 41 and the area outside the marked portion refers to region 4 in Figure 41. Here it is important to make sure, to scan the image of an experimentally disturbed Poly0 surface of the substrate (inside the marked portion shown in Figure 48) and also virgin Poly0 surface of the substrate (outside the marked portion) so that it is easy to measure the surface roughness of the both the substrate areas of an experimentally disturbed Poly0 surface of the substrate and also virgin Poly0 surface of the substrate. AFM image of a substrate with marked portion corresponding to regions 3 and 4 of Figure 41 is shown in Figure 48.

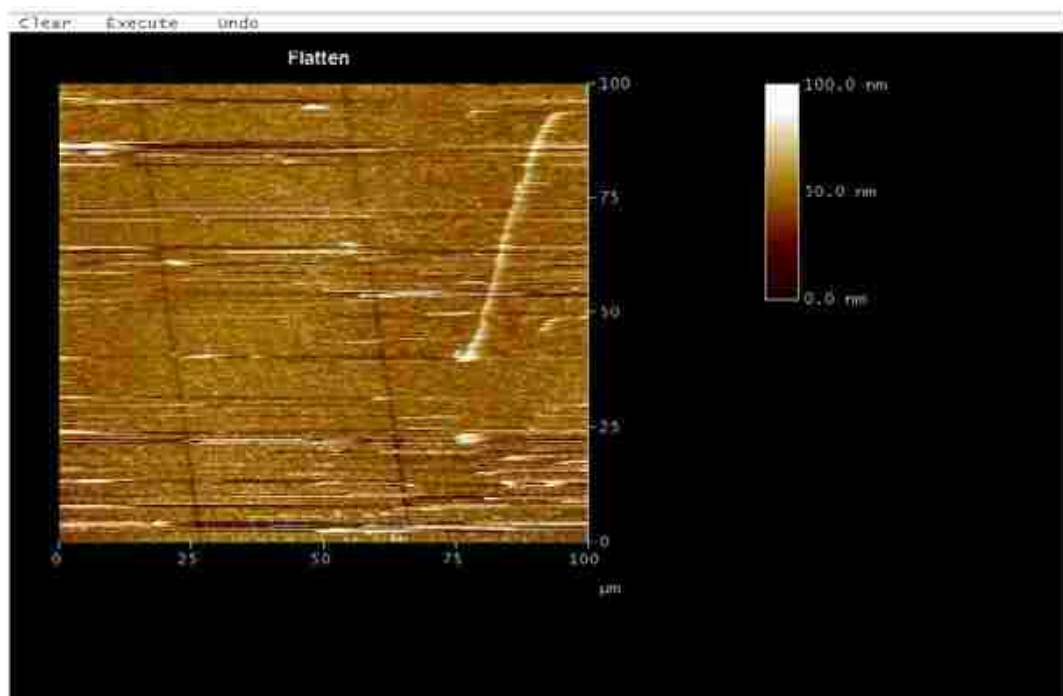


**Figure 48:** *AFM image of the substrate with marked region to identify contact and no contact areas with the bottom side of a  $\mu$ cantilever beam*

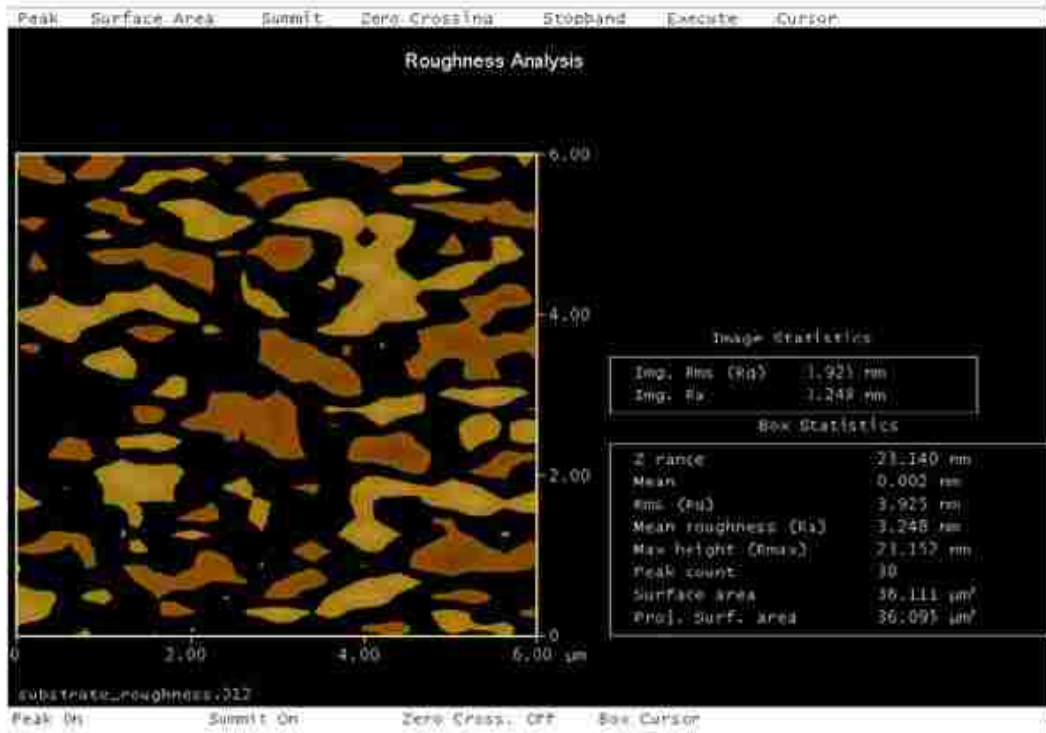


**Figure 49: AFM Roughness Analysis of an experimentally disturbed Poly0 surface of the substrate**

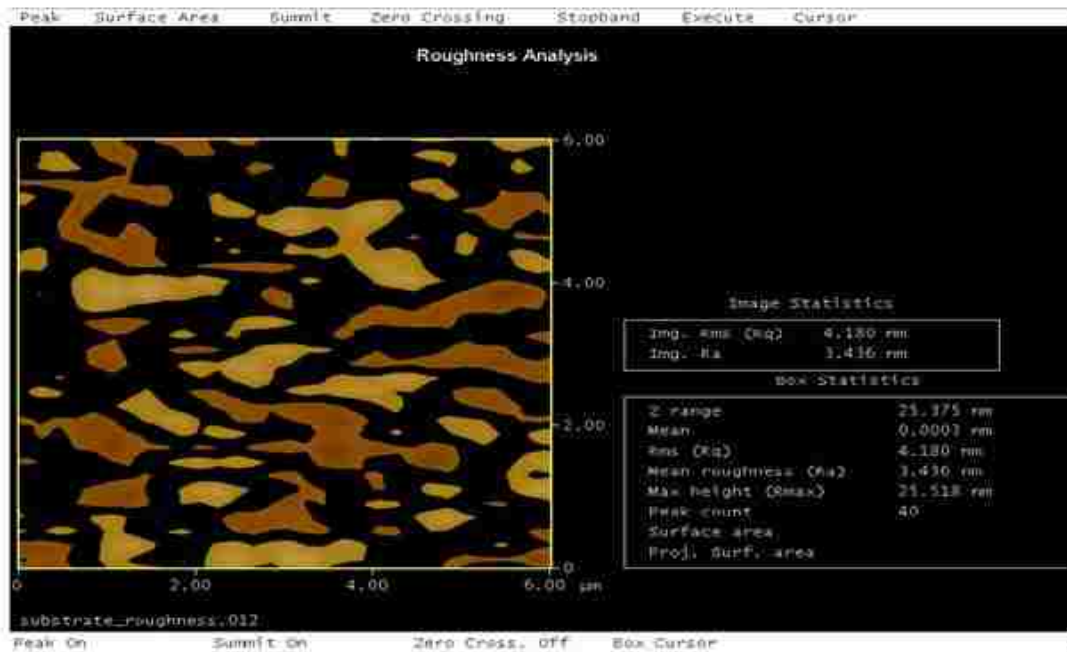


**Figure 50: AFM Roughness Analysis of a virgin Poly0 surface of the substrate**

For an experimentally disturbed Poly0 surface of the substrate, a RMS roughness of 3.925 nm was found which has almost same roughness value compared to the RMS roughness value of a virgin Poly0 surface of the substrate which is measured as 4.180 nm. No change in RMS roughness values is noticed due to the mechanical interlocking with a microcantilever beam. The peaks that broke off will sit in the valley of the bottom surface of the microcantilever beam causing no change in RMS roughness of a substrate. Thus, no change in surface roughness for an experimentally disturbed Poly0 surface of the substrate and a virgin Poly0 surface of the substrate is observed.

## CHAPTER 7

### CONCLUSIONS

#### 7.1 Conclusions Drawn from Mode I Experiments

In this work, a new method was developed for determining the total strain energy stored in  $\mu$ cantilevers, which both directly and indirectly includes the effects of all the forces as well as the moments present. The developed model is applicable for small deformations as well as large deformations. For small deformations, the developed model agrees well with common linear models but as the deformations increase, the two models start to deviate. Using the more sophisticated method developed here, the strain energy release rate was determined more accurately. Based on the experiments performed and using the models developed, the strain energy of poly-silicon / poly-silicon surfaces was found not to be a constant value but increased monotonically as the beams were peeled off of the surface. The strain energy release rate was found to be highly sensitive to parameters like the crack size and height, surface roughness, loading arrangement and friction. The maximum crack height studied was 14  $\mu\text{m}$ . Since most MEMS devices do not experience such large deflections, one can consider  $600 \text{ mJ}/\text{m}^2$  as an upper bound for the strain energy release rate for poly-silicon / poly-silicon MEMS surfaces. It was also found that due to the presence of noticeable longitudinal stresses, the so called Mode I crack propagation has some Mode II components too and is actually a mixed mode. As the height of the beam was increased, the effect of Mode II became more appreciable.

## 7.2 Conclusions Drawn from Mode II Experiments and Roughness Analysis

This work presents a novel technique to determine the Mode II interfacial adhesion energies. It is important to note that for the first time we developed an experimental method with which we can measure the interfacial energies from Mode II type failures. Separate new theories and experiments are developed to measure the upper bounds of  $G_{II}$  and also to determine a  $G_{II}$  value accurately. We measured the upper bounds of  $G_{II}$  as an average of  $G_{II} \leq 4.387 \text{ mJ/m}^2$ . And with the infinitesimal crack growth experiment, the accurate value of  $G_{II}$  is measured as  $0.932 \text{ mJ/m}^2$ . This value for Mode II is in-line for the mixed mode measurements made in sections previous to the Mode II experiments. The contribution of Mode II cannot be ignored in what is seemingly a Mode I type failure. This is attributed to the type of bonding between surface and roughness. As the surface roughness plays an important role in the adhesion of MEMS structures, the surfaces that were involved in the experiments are characterized with Atomic Force Microscopy (AFM). It is observed that the surface roughness of an experimentally disturbed Poly1 rubbed surface of  $\mu$ cantilever beam has more RMS roughness compared to a virgin Poly1 lower surface of  $\mu$ cantilever beam. The high value is reported as 63.992 nm and its counterpart as 24.949 nm. From the surface of microcantilever characterization, we conclude that the peaks broke off are sitting in the valley of the bottom surface of the microcantilever beam is the cause for a high RMS roughness value. At the same time, it is noticed that the surface roughness of an experimentally disturbed Poly0 surface of the substrate did not change when compared to the virgin Poly0 surface of the substrate. The RMS roughness of the substrate is found to be around 4 nm.

## REFERENCES

- [1] T. A. Core, W. K. Tsang and S. J. Sherman, "Fabrication Technology for an Integrated Surface-micromachined Sensor," *Solid State Technology*, vol. 36, pp.39, 1993.
- [2] P. F. Vankessel, L. J. Hornbeck, R. E. Meier and M. R. Douglass, "A MEMS-Based Projection Display," in *Proceedings of the IEEE, Hilton Head, SC*, pp. 1687-1704, 1998.
- [3] R. Hipwell, K. Bartholomew, W. Bonin, Z. E. Boutaghou and A. Lateef, "Hard disk drive performance enhanced by MEMS devices," in *Solid State Technology*, pp. 75-78, 2003.
- [4] S. Kamisuki, M. Fujii, T. Takekoshi, C. Tezuka and M. Atobe, "A High Resolution, Electronically-Driven Commercial Inkjet Head," in *IEEE*, 2000.
- [5] J. A. Geen, "Hilton Head '98," in *Hilton Head, SC*, pp. 51-54, 1998.
- [6] V. Aksyuk, "Hilton Head '98," in *Hilton Head, SC*, pp. 79-82, 1998.
- [7] M. S. Rodgers and J. J. Sniegowski, "Hilton Head '98," in *Hilton Head, SC*, pp. 144-149, 1998.
- [8] T. Abe, W. Messner and M. Reed, "Effective methods to prevent stiction during post-release-etch processing," in *Proceedings of IEEE MicroElectroMechanical Systems Conference, Amsterdam, The Netherlands*, pp. 94-99, 1995.
- [9] R. Legtenberg, J. Elders and M. Elwenspoek, "Stiction of surface microstructures after rinsing and drying: Model and investigation of adhesion mechanisms," in *Proceedings of Transducers 93, 7th International Conference of Solid-State Sensors and Actuators, Yokohoma, Japan*, pp. 198-201, 1993.

- [10] F. W. delRio, M. P. de-Boer, J. A. D. Reedy, P. J. Clews and M. L. Dunn, "The role of van der waals forces in adhesion of micromachined surfaces," *Nature Materials*, vol. 4, pp.629-634, 2005.
- [11] R. Maboudian and R. T. Howe, "Critical review: Adhesion in surface micromechanical structures," *Journal of Vacuum Science Technology B*, vol. 15, pp.1-20, 1997.
- [12] M. P. de-Boer, P. J. Clews, B. K. Smith and T. A. Michalske, "Adhesion of polysilicon microbeams in controlled humidity ambients," *Material Research Society Symposium Proceedings*, vol. 518, pp.131-136, 1998.
- [13] N. Fujitsuka and J. Sakata, "A new processing technique to prevent stiction using silicon selective etching for SOI-MEMS," *Sensors and Actuators A, Physics*, vol. 97-98, pp.716-719, 2002.
- [14] G. T. Mulhern, D. S. Soane and R. T. Howe, "Supercritical carbondioxide drying of microstructures," in *Proceedings of the 7th International Conference on Solid-State Sensors and Actuators, Yokohama*, pp. 296-299, 1993.
- [15] C. H. Mastrangelo and G. Saloka, "A dry-release method based on polymer columns for microstructure fabrication," in *Proceedings of the IEEE MicroElectroMechanical Systems Workshop, Fort Lauderdale, FL*, pp. 77-81, 1993.
- [16] M. Orpana and A. O. Korhonen, "Control of residual stress of polysilicon thin films by heavy doping in surface micromachining," in *Proceedings of the 6th International Conference on Solid-State Sensors and Actuators, San Franscisco*, pp. 957-960, 1991.



- [17] J. H. Lee, H. H. Chung, S. Y. Kang, J. T. Baek and H. J. Yoo, "Fabrication of surface micromachined polysilicon actuators using dry release process of HF gas-phase etching," in *Proceedings of the International Electron Devices Meeting, San Francisco*, pp. 761-764, 1996.
- [18] P. J. Resnick and P. J. Clews, "Whole wafer critical point drying of MEMS devices," in *Proceedings of the SPIE International Society for Optical Engineering Meeting, Bellingham, WA*, pp. 189-196, 2001.
- [19] J. Anguita and F. Briones, "HF/ H<sub>2</sub>O vapor etching of SiO<sub>2</sub> sacrificial layer for large-area surface-micromachined membranes " *Sensors and Actuators A, Physics*, vol. 64, pp.247-251, 1998.
- [20] F. Kozlowski, N. Lindmair, T. H. Scheiter, C. Hierold and W. Lang, "A novel method to avoid sticking of surface micromachined structures," in *Proceedings of the 8th International Conference on Solid-State Sensors and Actuators, Stockholm*, pp. 220-223, 1995.
- [21] H. Guckel, J. Sniegowski, T. Christenson and F. Raissi, "The application of fine-grained polysilicon to mechanically resonant transducers," *Sensors and Actuators A, Physics*, vol. 21-23, pp.346-351, 1990.
- [22] R. L. Alley, G. J. Cuan, R. T. Howe and K. Komvopoulos, "The effect of release-etch processing on surface microstructure stiction," in *Proceedings of the IEEE Solid-State Sensors and Actuators Workshop, Hilton Head, SC*, pp. 202-207, 1992.
- [23] W. R. Ashurst, C. Yau, C. Carraro, C. Lee, G. J. Kluth, R. T. Howe and R. Maboudian, "Alkene based monolayer films as anti-stiction coatings for

- polysilicon MEMS," *Sensors and Actuators A, Physics*, vol. 91, pp.239-248, 2001.
- [24] W. R. Ashurst, C. Yau, C. Carraro, R. Maboudian and M. T. Dugger, "Dichlorodimethylsilane as an anti-stiction monolayer for MEMS: A comparison to the octadecyltrichlorosilane self-assembled monolayer," *Journal of Microelectromechanical Systems*, vol. 9, pp.41-49, 2001.
- [25] R. Maboudian, W. R. Ashurst and C. Carraro, "Self-assembled monolayers as anti-stiction coating for MEMS: Characteristics and recent progress," *Sensors and Actuators A, Physics*, vol. 82, pp.219-223, 2000.
- [26] B. J. Kim, M. Liebau, J. Huskens, D. N. Reinhoudt and J. Brugger, "A self-assembled monolayer-assisted surface microfabrication and release technique," *Microelectronic Engineering*, vol. 57-58, pp.755-760, 2001.
- [27] U. Srinivasan, M. R. Houston, R. T. Howe and R. Maboudian, "Alkyltrichlorosilane-based self-assembled monolayer films for stiction reduction in silicon micromachines," *Journal of Microelectromechanical Systems*, vol. 7, pp.252-260, 1998.
- [28] U. Srinivasan, M. R. Houston, R. T. Howe and R. Maboudian, "Self-assembled fluorocarbon films for enhanced stiction reduction," in *Proceedings of the 9th International Conference on Solid-State Sensors and Actuators, Chicago*, pp. 210-213, 1997.
- [29] K. M. Hurst, C. B. Roberts and W. R. Ashurst, "Gas-expanded liquid nanoparticle deposition technique to reduce adhesion of silicon microstructures," *Nanotechnology*, vol. 20:185303, pp.1-9, 2009.

- [30] K. Deng, R. J. Collins, M. Mehregany and C. N. Sukenik, "Performance impact of monolayer coating of polysilicon microstructures," in *Proceedings of the IEEE Micro Electro Mechanical Systems Workshop, Amsterdam*, pp. 368-373, 1995.
- [31] J. W. Rogers and L. M. Phinney, "Process Yields for Laser Repair of Aged, Stiction-Failed, MEMS Devices," *Journal of Microelectromechanical Systems*, vol. 10, pp.280-285, 2001.
- [32] J. W. Rogers and L. M. Phinney, "Nanoscale laser repair of aged stiction-failed MEMS devices," *Journal of Heat Transfer*, vol. 124, pp.394-396, 2002.
- [33] J. W. Rogers, T. J. Mackin and L. M. Phinney, "A Thermomechanical Model for Adhesion Reduction of MEMS Cantilevers," *Journal of Microelectromechanical Systems*, vol. 11, pp.512-520, 2002.
- [34] L. M. Phinney and J. W. Rogers, "Pulsed laser repair of adhered, surface-micromachined, polycrystalline silicon cantilevers," *Journal of Adhesion Science Technology*, vol. 17, pp.603-622, 2003.
- [35] V. Kaajakari and A. Lal, "Pulsed Ultrasonic Release and Assembly of Micromachines," in *10th International Conference on Solid-State Sensors and Actuators*, pp. 212-215, 1999.
- [36] V. Kaajakari, S. H. Kan, L. J. Lin, A. Lal and S. Rodgers, "Ultrasonic Actuation for MEMS Dormancy Related Stiction Reduction," *Proceedings of SPIE*, vol. 4180, pp.60, 2000.
- [37] V. Gupta, R. Snow, M. C. Wu, A. Jain and J. C. Tsai, "Recovery of Stiction-Failed MEMS Structures Using Laser-Induced Stress Waves," *Journal of Microelectromechanical Systems*, vol. 13, pp.696-700, 2004.

- [38] Z. C. Leseman, S. B. Koppaka and T. J. Mackin, "A fracture mechanics description of stress-wave repair in stiction-failed microcantilevers: Theory and Experiments " *Journal of Microelectromechanical Systems*, vol. 16, pp.904-911, 2007.
- [39] A. A. Savkar, K. D. Murphy, Z. C. Leseman, T. J. Mackin and M. R. Begley, "On the Use of Structural Vibrations to Release Stiction Failed MEMS," *Journal of Microelectromechanical Systems*, vol. 16, pp.163-173, 2007.
- [40] D. F. Goettler, M. R. Kashamolla, Z. C. Leseman, A. A. Savkar and K. D. Murphy, "Repair of Stiction Failed MEMS Using Structural Vibrations," in *Proceedings of the 2008 ASEE Gulf-Southwest Annual Conference, Albuquerque, New Mexico*, Session 12-24, 2008.
- [41] C. H. Mastrangelo and C. H. Hsu, "A simple experimental technique for the measurement of the work of adhesion of microstructures," in *Proceedings of International Workshop Solid-State Sensors and Actuators, Hilton Head, SC*, pp. 208-212, 1992.
- [42] C. H. Mastrangelo and C. H. Hsu, "Mechanical stability and adhesion of microstructures under capillary forces - Part I: Basic theory," *Journal of Microelectromechanical Systems*, vol. 2, pp.33-43, 1993.
- [43] C. H. Mastrangelo and C. H. Hsu, "Mechanical stability and adhesion of microstructures under capillary forces - Part II: Experiments," *Journal of Microelectromechanical Systems*, vol. 2, pp.44-55, 1993.
- [44] M. P. de-Boer and T. A. Michaske, "Accurate method for determining adhesion of cantilever beams," *Journal of Applied Physics*, vol. 86, pp.817-827, 1999.

- [45] E. Jones, M. Begley and K. Murphy, "Adhesion of micro-cantilevers subjected to mechanical point-loading: Modeling and experiments," *Journal of Mech. Phys. Solids*, vol. 51, pp.1601-1622, 2003.
- [46] Z. C. Leseman, S. P. Carlson and T. J. Mackin, "Experimental Measurements of the Strain Energy Release Rate for Stiction-Failed Microcantilevers Using a Single-Cantilever Beam Peel Test," *Journal of Microelectromechanical Systems*, vol. 16, pp.38-43, 2007.
- [47] Z. C. Leseman, S. Carlson, X. Xue and T. J. Mackin, "A Standard Approach For Measuring Adhesion Energies In Stiction-Failed Microdevices," in *ASME International Mechanical Engineering Congress and Exposition, Chicago, Illinois USA*, pp. 1-9, 2006.
- [48] K. M. Hurst, C. B. Roberts and W. R. Ashurst, "A New Method to Determine Adhesion of Cantilever beams Using Beam Height Experimental Data," in *Tribol Lett.*, 2009.
- [49] R. Frisch-Fay, "Flexible Bars," Ryde, New South wales, Australia: Butterworths & Co. Limited, 1962.
- [50] M. P. de-Boer, "Thermodynamics of capillary adhesion between rough surfaces," *Journal of Colloid and Interface Science*, vol. 311, pp.171-185, 2007.
- [51] W. R. Ashurst, M. P. de-Boer, C. Carraro and R. Maboudian, "An investigation of sidewall adhesion in MEMS," *Applied Surface Science*, vol. 212-213, pp.735-741, 2003.

- [52] A. K. Mousavi, M. R. Kashamolla and Z. C. Leseman, "Improved Model for the Adhesion of  $\mu$ cantilevers: Theory and Experiments," *Journal of Microelectromechanical Systems*, vol. (yet to be published), 2010.
- [53] K. Abbas, "Design Fabrication and Calibration of MEMS Actuators for In-situ Materials Testing," *Master's Thesis, Department of Mechanical Engineering, University of New Mexico, Albuquerque, 2008.*
- [54] W. C. Young, "Roark's Formulas for Stress and Strain," *6th ed.*, McGraw Hill, 1989.
- [55] H. L. Ewalds and R. J. H. Wanhill, "Fracture Mechanics," New York: Edward Arnold, 1993.
- [56] J. J. Sniegowski and M. P. de-Boer, "IC-compatible polysilicon surface micromachining," *Annual Review Material Science*, vol. 30, pp.299-333, 2000.
- [57] M. P. de-Boer, D. L. Luck, W. R. Ashurts, R. Maboudian, A. D. Corwin and J. A. Walraven, "High-performance surface-micromachined inch-worm actuator," *Journal of Microelectromechanical Systems*, vol. 13, pp.63-74, 2004.
- [58] Z. C. Leseman, "A Novel method for testing freestanding nanofilms using a custom MEMS load cell," *PhD. Dissertation, Department of Mechanical Engineering, University of Illinois, Urbana-Champaign, 2006.*
- [59] F. Larmer and A. Schilp, "Method for anisotropically etching silicon," *Patent DE4241045, US 5501893, and EP 625285, 1992.*
- [60] C. K. Bora, M. D. Street, J. M. Redmond, M. J. Starr, R. W. Carpick and M. E. Plesha, "Multiscale roughness and modeling of MEMS interface," *Tribology Letters*, vol. 19, pp.37-48, 2005.

- [61] X. Xue and A. A. Polycarpou, "An improved meniscus surface model for contacting rough surfaces," *Journal of Colloid and Interface Science*, vol. 311, pp.203-211, 2007.
- [62] -----, "Meniscus model for noncontacting and contacting sphere-on-flat surfaces including elastic-plastic deformation," *Journal of Applied Physics*, vol. 103, 2008.
- [63] D. Maugis, "On the contact and adhesion of rough surfaces," *Journal of Adhesion Science Technology*, vol. 10, pp.161-175, 1996.
- [64] K. Deng and W. H. Ko, "A study of static friction between silicon and silicon compounds," *Journal of Micromech. Microengineering*, vol. 2, pp.14-20, 1992.
- [65] M. F. Ashby and D. R. H. Jones, "Engineering Materials 1," 3rd ed., Butterworth Heinemann, 2005.